Integrated design optimization method for novel vapour-compression-cycle-based environmental control systems

Ascione, F.; Colonna, P.; De Servi, C. M.

DOI
10.1016/j.applthermaleng.2023.121261

Publication date
2024

Document Version
Final published version

Published in
Applied Thermal Engineering

Citation (APA)
Ascione, F., Colonna, P., & De Servi, C. M. (2024). Integrated design optimization method for novel vapour-compression-cycle-based environmental control systems. *Applied Thermal Engineering*, *236*, Article 121261. https://doi.org/10.1016/j.applthermaleng.2023.121261

Important note
To cite this publication, please use the final published version (if applicable).
Please check the document version above.

Applied Thermal Engineering 236 (2024) 121261

Contents lists available at ScienceDirect

Applied Thermal Engineering

journal homepage: www.elsevier.com/locate/ate

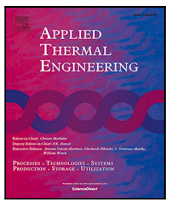

Research Paper

Integrated design optimization method for novel vapour-compression-cycle-based environmental control systems

F. Ascione [a], P. Colonna [a], C.M. De Servi [a,b,*]

[a] Propulsion and Power, Delft University of Technology, Kluyverweg 1, Delft, 2629 HS, The Netherlands
[b] Energy Technology Unit, VITO, Boeretang 200, BE-2400, Mol, Belgium

ARTICLE INFO

Keywords:
Integrated design optimization
Environmental control system
Helicopter/aircraft auxiliary systems
More electric aircraft/rotorcraft
Vapour compression cycle
High-speed centrifugal compressor

ABSTRACT

The aircraft Environmental Control System (ECS) is the primary consumer of non-propulsive power at cruise conditions, hence, its performance optimization is crucial for the reduction of specific fuel consumption. A novel integrated system design optimization method is presented: thermodynamic cycle, component sizing and working fluid are taken into account simultaneously. This method was applied to the ECS of large rotorcraft based on a Vapour Compression Cycle system electrically driven by a high-speed centrifugal compressor. Steady-state and lumped parameter system component models have been developed using the Modelica acausal modelling language. The optimization design framework consists of an in-house code, featuring a Python-Modelica interface. The study case refers to a critical operating condition: the helicopter is on the ground during a hot and humid day. The working fluid is R-134a. The multi-objective optimization targets the maximization of the system efficiency and the minimization of system weight. The results show that more efficient systems can be designed only with heavier components. The design feasibility of high-speed centrifugal compressors is demonstrated. The advantage of an integrated system design optimization framework for complex energy systems is proved, allowing for the analysis of the impact of both component design and working fluid on system performance.

1. Introduction

The significant air traffic growth, observed in the last decades and expected to increase in the upcoming years, has raised the urgency for the aerospace industry to increase the sustainability of air transport technologies. FlightPath 2050 [1], a report published by the Advisory Council for Aviation Research and innovation in Europe (ACARE), provides a roadmap for the reduction of the environmental impact, and in particular for cutting CO_2 emissions by improving aircraft fuel efficiency. In this regard, the electrification of all non-propulsive components may provide considerable improvements in terms of aircraft weight, fuel consumption, total life cycle costs, controllability and maintainability of future-generation vehicles. This paradigmatic change of non-propulsive equipment is at the basis of the More Electric Aircraft (MEA) concept [2].

The auxiliary system supplying cabin pressurization and thermal comfort, hereinafter indicated as Environmental Control System (ECS), is currently the primary consumer of non-propulsive energy at cruise conditions [3]. The ECS must ensure the correct supply of air and temperature control of cabin and cockpit, even for the most critical environmental conditions, not only for passengers comfort, but also for avionics reliability.

This study is part of a research project about a novel concept of aircraft ECS to reduce the associated non-propulsive power consumption. In particular, the work documented in this article focuses on the development of a method for the optimal preliminary design of such ECS. The method is tested by applying it to the design of the ECS of a high-payload rotorcraft. The ECS adopts a Vapour Compression Cycle (VCC) system for cabin cooling and it features an electrically driven high-speed centrifugal compressor as prime mover, instead of the currently adopted scroll machines. The compressor is under development and its optimized design is part of another work package of the project. The working fluid selected for this study is the commonly employed R-134a refrigerant.

The ECS onboard helicopters consists of two sub-systems: one for cabin heating and another for cooling. Cabin heating is obtained by mixing air bled from the engine with outside air, while cabin cooling is achieved either by means of an Air Cycle Machine (ACM) or a VCC system. The thermodynamic efficiency of VCC systems is considerably higher than that of ACMs, however, VCC systems tend to be heavier [4].

* Corresponding author at: Propulsion and Power, Delft University of Technology, Kluyverweg 1, Delft, 2629 HS, The Netherlands.
E-mail addresses: f.ascione@tudelft.nl (F. Ascione), p.colonna@tudelft.nl (P. Colonna), c.m.deservi@tudelft.nl (C.M. De Servi).

https://doi.org/10.1016/j.applthermaleng.2023.121261
Received 8 February 2023; Received in revised form 24 July 2023; Accepted 31 July 2023
Available online 15 August 2023

Nomenclature

Acronyms

AM	Angular Momentum per unit of mass
DeSimECS	Design and Simulation of Energy Conversion Systems
ACM	Air Cycle Machine
CHEX	Compact Heat Exchanger
COP	Coefficient Of Performance
CV	Control Volume
DAE	Differential Algebraic Equation
ECS	Environmental Control System
FV	Finite Volume
GWP	Global Warming Potential
HEX	Heat Exchanger
HFC	Hydrofluorocarbon
IRIS	Inverse organic Rankine cycle Integrated System
ITMS	Integrated Thermal Management System
MB	Moving Boundary
MEA	More Electric Aircraft
MGB	Main Gear Box
NTU	Number of Thermal Units
ODP	Ozone Depletion Potential
OVAT	One Variable At a Time
PHEX	Plate Heat Exchanger
R-134a	1,1,1,2-Tetrafluoroethane
VCC	Vapour Compression Cycle

Greek Symbols

α_2	Impeller outlet absolute angle (°)
$\beta_{1,s}$	Inlet blade metal angle at shroud (°)
β_{plate}	Plate inclination angle (°)
δ_f	Fins thickness (m)
δ_{mc}	Minichannel thickness (m)
δ_{pipe}	Pipe wall thickness (m)
δ_t	Flat tube thickness (m)
δ_{plate}	Flat plate thickness (m)
ϵ	Effectiveness (–) - Relative roughness (–)
γ_{Pv}	Isentropic pressure-volume exponent (–)
Λ	Amplitude sinusoidal corrugation pattern (m)
μ	Dynamic viscosity (Pa s)
Ω	Rotational speed (rpm)
Φ	Two-phase multiplier
Φ'	Modified mass flow function (–)
Φ_t	Compressor swallowing capacity (–)
Ψ	Compressor loading coefficient (–)
ρ	Density (kg/m^3)
σ_{max}	Maximum allowable material stress (Pa)
Θ	Louver angle (°)

Subscripts

1	Compressor impeller inlet
2	Compressor impeller outlet
3	Compressor diffuser inlet
4	Compressor diffuser outlet
air	Air stream
cb	Cabin
compr	Compressor
cond	Condenser
cr	Critical
env	Environmental
eva	Evaporator
fan	Ram air fan
fresh	Fresh air stream
h	Hydraulic
i	Internal
int	Intermediate
intcool	Intercooler
L	Liquid phase
out	Outlet
pp	Pinch-point
ram	Ram air stream
rec	Recirculated air stream
s	Impeller shroud
S1	First stage compressor
S2	Second stage compressor
sat	Saturation
tot	Total thermodynamic property
u	Tangential component of the velocity
V	Dry vapour phase

Non Dimensional Numbers

Bo	Boiling number
Co	Convection number
Fr	Froude number
M_{u_2}	Outlet tip Mach number
$M_{w_{1,s}}$	Inlet relative Mach number at shroud
Nu	Nusselt number
Pr	Prandtl number
Re	Reynolds number
Re_x	Reynolds number based on logarithmic spiral trajectory through the diffuser
Re_{Lp}	Reynolds number based on the louver pitch
We	Weber number

Roman Symbols

$\dot{m}$	Mass flow rate (kg/s)
$\dot{Q}$	Thermal power (W)
$\dot{V}$	Volumetric flow rate (kg/(m^3 s))
$\dot{W}$	Mechanical power (W)
$C_1 - C_5$	Constant parameters
F_{fl}	Fluid dependent parameter
$N_{channel}$	Number of channels per pass (–)
N_{pass}	Number of passes (–)
a	Wave length corrugation pattern (m)
b	Fin height (m)
c	Absolute flow velocity (m/s)
C_f	Skin friction coefficient (–)
c_u	Tangential component of the absolute velocity (m/s)
C_p	Diffuser pressure recovery factor (–)
D	Diameter - Heat exchanger depth (m)
d	Diffuser width (m)
D_{out}	Outer pipe diameter (m)
D_{port}	Port diameter (m)
F	Force (N)

f	Friction factor (–)
F_d	Fin depth (m)
F_p	Fin pitch (m)
H	Heat exchanger height (m)
h	Heat transfer coefficient (W/(m^2 K)) - Specific enthalpy (J/kg)
j	Colburn factor (–)
k	Thermal conductivity (W/(m K)) - Compressor shape factor (–)
l	Tube length (m)
L_h	Louver height (m)
L_l	Louver length (m)
L_{plate}	Plate length (m)
L_p	Louver pitch (m)
M_r	Molecular weight (–)
$n = 0.25$	Constant (–)
p	Pressure (Pa)
p_{gauge}	Gauge pressure (Pa)
P_t	Tube pitch (m)
q	Heat flux (J/m^2)
R	Radius (m)
Ra	Absolute roughness (μm)
s	Slip ratio (–)
T	Temperature (K)
T_h	Tube height (m)
T_p	Tube pitch (m)
U	Overall heat transfer coefficient (W/(m^2 K))
u	Impeller blade speed (m/s)
W	Heat exchanger width (m)
W_f	Dissipated specific work due to friction (J/kg)
W_{plate}	Flat plate width (m)
x	Vapour quality (–)
$y = 0.4$	Sizing coefficient (–)
K	Constant (–)
N_{bl}	Number of blades (–)

Recently, many research attempts to improve the performance of rotorcraft ECS have been documented. These studies focused on assessing different system configurations featuring various working fluids. Zilio et al. [5] investigated a new cooling setup for helicopter avionics, adopting a mini-VCC system and a loop heat pipe. Pang et al. [6] described an Integrated Thermal Management System (ITMS) for helicopters, capable of satisfying both cabin heating and cooling demand. The system is also based on heat pump technology. In particular, on cold days, waste heat from the lubricating oil system is recovered, without bleeding hot air from the engine. On hot days, the system is switched to a classical refrigeration cycle, using a three-way valve. The authors evaluated the system performance in terms of exergy, efficiency and fuel weight penalty. The considered system model does not include detailed models of all the components of each subsystem. Mannini [7] designated the total system weight and the total absorbed power as critical indicators to properly analyse the optimal ECS configuration for rotorcraft. The effect of these two criteria can be evaluated with one single design variable, namely the payload penalty, whose minimization is the objective of the system optimization. The author demonstrates that for large rotorcraft, the optimal ECS configuration is generally based on the VCC concept, as it results in a lower fuel payload penalty thanks to its higher conversion efficiency with respect to the ACM [8].

Other relevant research about ECS mainly concerns the design optimization of the ACM onboard airplanes. Vargas and Bejan [9] proposed an integrated system optimization method for the ECS of commercial airplanes, whereby both the cycle operating parameters and the preliminary design of the heat exchangers are considered within the optimization procedure. The exergy destruction associated with performance and weight of the ECS is minimized. This approach not only allows for the definition of an optimal system operating point but also for the design analysis of the most critical components within the system, e.g., the heat exchangers. Using the same approach, Pérez-Grande and Leo [10] describe the results of a multi-objective optimization of a bleed-less ACM. The functions to be minimized are the system weight and the entropy generation. However, their study focuses solely on the geometrical design and thermodynamic characterization of the two heat exchangers. Finally, Sielemann et al. [11] described an integrated design optimization methodology for an unconventional aircraft ECS architecture, coupling the features of the ACM and of the VCC systems. The models of the main system components are developed using the equation-based object-oriented Modelica language [12]. The system is optimized by accounting for the minimization of two objective functions, namely the additional specific fuel consumption and the weight associated with the ECS at cruise conditions. The authors draw conclusions about the influence of the heat exchangers geometrical design on the specific fuel consumption related to the ECS. However, the study neglects the turbomachinery preliminary design and the analysis of its impact on the overall system performance and design.

All the mentioned literature proposes methods for the optimization of ECS performance, accounting at the same time for the design of the main system components. However, the analysis is usually limited to the detailed design of the heat exchangers, and turbomachinery is simply treated by assuming constant values of isentropic efficiency to roughly determine the system power consumption. The objective of the current work is to bridge this knowledge gap by proposing an integrated optimal design method relying on a detailed mean-line approach for turbomachinery preliminary design. The selected optimization test case concerns the ECS of a large helicopter, encompassing at the same time the thermodynamic cycle, the working fluid choice, and the detailed design of all the main system components, i.e., the heat exchangers, the piping and the centrifugal compressor. Furthermore, this method is applied to a novel concept of VCC system for helicopter ECS, whose prime mover is an electrically-driven high-speed centrifugal compressor instead of the traditional mechanically-driven scroll compressor. The system model comprises lumped parameter component models implemented in an acausal modelling language [12]. The design feasibility of such technology is analysed by performing a system optimization whose objective functions are the system weight and efficiency.

This article is structured as follows. First, the VCC system for rotorcraft ECS is described. Then, the preliminary design methodology of all the components of the system is illustrated in detail. Next, the multi-objective integrated design optimization framework is explained, the objective functions are stated, and the design space of the problem and its constraints are defined. The results obtained by applying the optimal design method are then discussed with an emphasis on the design feasibility of the high-speed centrifugal compressor. Finally, the main outcomes of the study are summarized in the conclusions, together with an outlook on future work.

2. Vapour compression system

The typical VCC system onboard large rotorcraft employs a scroll compressor (Fig. 1). The working fluid is commonly the hydrofluorocarbon (HFC) R-134a. This refrigerant is neither flammable nor toxic and its Ozone Depletion Potential (ODP) is null [13]. Thanks to these properties, the ARP731C [14] indicated R-134a as one of the most suitable refrigerants in VCC systems for aircraft applications. Two

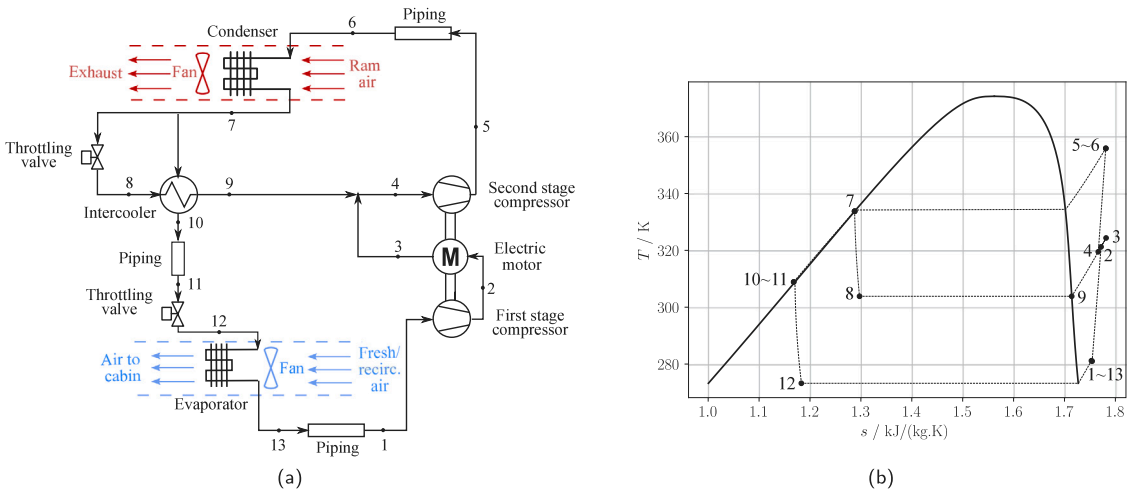

Fig. 1. (a) Process flow diagram of an ECS for helicopters and (b) the corresponding representation of the thermodynamic cycle in the *T-s* chart of the fluid (R-134a).

separate VCC systems provide cooling to the cabin and the cockpit. Each refrigeration loop is equipped with a dedicated condenser with an independent cooling air intake and fan. The cycle configuration includes an intercooler, i.e., a heat exchanger (HEX) used to sub-cool the refrigerant entering the expansion valve upstream of the evaporator. In this way, the vapour quality of the refrigerant entering the evaporator decreases. For a prescribed cooling capacity, the resulting refrigerant mass flow rate decreases, thus improving the system performance [8]. The baseline VCC system selected for this study, namely the one currently adopted for many rotorcraft models, uses a mechanically driven scroll compressor to pressurize the working fluid. The scroll compressor features an intercooled compression: the mass flow rate of superheated refrigerant vapour from the intercooler is injected into the compressor at a pressure level that is intermediate between the evaporation and the condensation pressure of the system. Once injected, the refrigerant mixes with the hotter vapour flowing through the compressor, thus decreasing the overall fluid temperature. Downstream the vapour injection, the compressor operates with a higher mass flow rate of refrigerant, which is further compressed until the target condensation pressure is reached. The condenser is made up of three flat-tube minichannel heat exchangers in parallel on the refrigerant side and in series on the air side. The same type of heat exchanger is adopted for the evaporator. The air entering the evaporator is, to a significant extent, recirculated from the cabin and the cockpit. To ensure passengers comfort, the ARP292 [15] standard prescribes that each occupant should be provided with a fresh air mass flow rate of at least 4.5 g/s in the cabin and 5.6 g/s in the cockpit, while air humidity should not exceed 65%. According to the same reference, due to the helicopter low flying altitude, a cabin air pressurization system is not necessary. Hence, the ratio of recirculated to fresh air is remarkably high with respect to a typical aircraft ECS. A filter is eventually added in front of the evaporator to avoid contamination of cabin air with sand, dust or other pollutants from the environment. Both the condenser and the evaporator fans are electrically driven.

The novel VCC system benchmarked against the baseline case features an electrically driven and oil-free centrifugal compressor instead of the traditional mechanically-driven scroll machine. Two compression stages are necessary, given the required difference between the operating pressure of the condenser and that of the evaporator. The two compressors are mounted in a back-to-back configuration on the same shaft to minimize the axial thrust of the gas bearings. This compressor is characterized by values of isentropic efficiency reaching up to 85%, which make this technology an attractive alternative to scroll compressors whose efficiency never exceeds 70% [16]. Fig. 2 provides a schematic of the installation arrangement of the ECS components onboard the helicopter. The scroll compressor is always located in the upper part of the vehicle, connected to a mechanical drive of the Main Gear Box (MGB). The three condensers are also installed in this area of the helicopter, but in a separate compartment, to minimize the temperature rise in the cooling air due to heat losses from the propulsion system. The cockpit evaporator is situated under the floor within the nose of the helicopter, while the cabin evaporator is usually located in the aft. The location of the scroll compressor implies the need for a long pipe to connect the evaporator outlet to the compressor suction port. This hose can reach up to 4 – 6 m, thus negatively impacting the overall system performance because of the large associated refrigerant pressure drop, especially in the case of low-density working fluids. In this regard, the electrically driven centrifugal compressor solution offers the advantage of higher flexibility of installation, which can lead to a different positioning of the turbomachinery, closer to the evaporator.

3. Models

The electrically-driven VCC system was modelled using the equation-based, acausal, object-oriented Modelica language [12]. The Modelica language, being acausal, allows for the use of the same model of a component for both on-design and off-design simulations. The in-house library *DeSimECS* (Design and Simulation of Energy Conversion Systems) featuring multi-domain lumped-parameters models of components, e.g., thermal, hydraulic, mechanical, and electrical components for steady-state simulations was further developed for this purpose. All the models are mathematically described by systems of non-linear algebraic equations including conservation and constitutive equations. Component models can be assembled together to build systems of different complexity.

In this study, system simulations were used to evaluate relevant operating parameters, system performance and, at the same time, for the preliminary design of the main components, i.e., the centrifugal compressor, the heat exchangers, and the piping lines. The working fluid is R-134a, whose thermodynamic and transport properties have been calculated using a well-known commercial program [17].

3.1. Heat exchangers

The helicopter ECS includes three heat exchangers, i.e., condenser, evaporator and intercooler. The need for lightweight and high thermally efficient systems calls for the adoption of compact heat exchangers (CHEXs) [18].

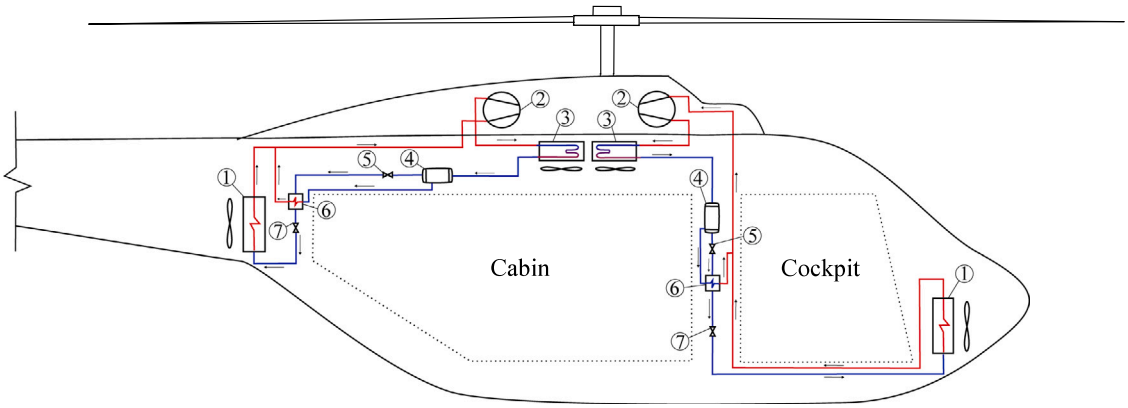

Fig. 2. Installation arrangement of the Environmental Control System components onboard the helicopter: (1) Evaporator, (2) Compressor, (3) Condenser unit, (4) Liquid tank, (5) Expansion valve, (6) Intercooler, (7) Expansion valve.

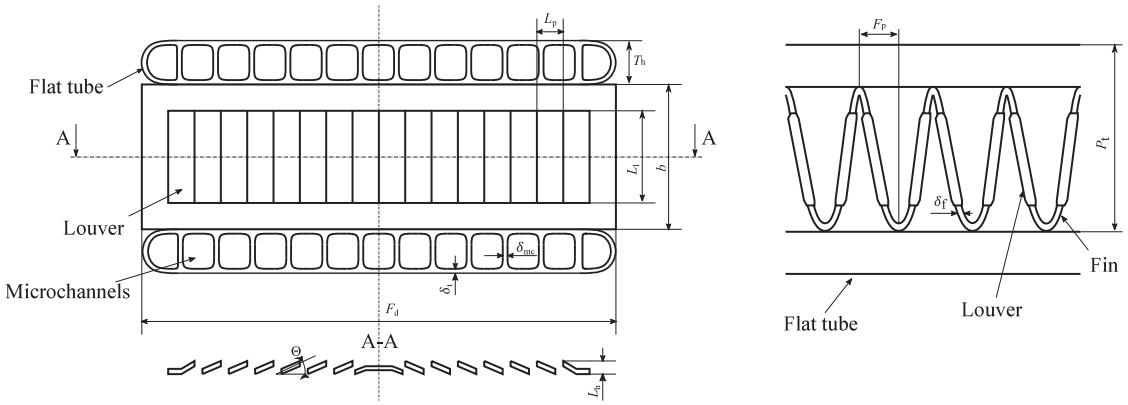

Fig. 3. Minichannel flat tubes and multilouvered fins HEX geometry.

3.1.1. Condenser and evaporator

The condenser and the evaporator are finned-tube CHEXs. The working fluids, namely air and refrigerant, circulate according to a cross-flow arrangement. More specifically, the refrigerant flows into flat tubes featuring small internal passages, i.e., minichannels with rectangular section (the hydraulic diameter ranges from 3 mm to 0.2 mm [19]), while the air flows outside the channels. The fins are of the multi-louvered type: several louvers along the fin length increase the heat transfer surface on the air side. The continuous breaking of the boundary layer of the flow passing through the louvers promotes the enhancement of the heat transfer coefficient by two to four times with respect to unlouvered surfaces of the same dimensions. The CHEXs equipping helicopter ECS are derived from the CHEXs employed on board automotive vehicles as radiators and their typical compactness factor is around 1100 m^2/m^3 [18]. Fig. 3 shows the main geometrical parameters of the CHEX core. Its geometrical characterization, as well as the weight estimation, are based on the guidelines by Shah and Sekulić [20]. The condenser model implemented in the *DeSimECS* library has been validated by comparing the numerical results to the outcome of the experimental campaign documented in the work by Kim and Bullard [21], who tested microchannel condensers for a room air conditioning system. The results show a discrepancy lower than 4% in the calculation of the heat transfer surface and a 10% deviation in the estimation of the pressure drop. It was not possible to carry out a comparison in terms of heat transfer coefficient, as this quantity was not reported in the aforementioned study.

The HEXs are critical components for what concerns the evaluation of the performance and the weight of a rotorcraft ECS, hence their models should achieve an optimal trade-off between results accuracy and numerical complexity. The Moving Boundary (MB) method has been preferred to a Finite Volume (FV) discretization method as it allows for lower computational cost without compromising model accuracy, as demonstrated by Bendapudi et al. [22]. The MB models of the evaporator and condenser are obtained by dividing the HEX length in a number of control volumes equal to the number of thermodynamic phases of the refrigerant. The evaporator features two control volumes (CVs) for the refrigerant side, namely a two-phase flow (evaporation) CV and a dry vapour (superheating) CV. Mass and energy balance equations are solved for each control volume, whose length depends on the refrigerant vapour quality. The main modelling assumptions are: (i) both the refrigerant and the air flow rate are one-dimensional; (ii) the specific enthalpy distribution is linear with the length within each CV, therefore thermodynamic properties are computed as an average of the ones at the inlet and the outlet of each CV; (iii) the void fraction of the two-phase flow refrigerant is calculated by assuming that the homogeneous flow model holds. More specifically, the slip ratio (s), expressed as the ratio between the velocity of the gaseous flow (c_V) to the velocity of the liquid (c_L), is assumed equal to one, meaning that the two flow phases are perfectly mixed [23]; (iv) the air outlet temperature is computed according to the assumption of ideal mixing of the air streams exiting each control volume.

Heat transfer coefficient and pressure drop are evaluated using specific correlations for each refrigerant phase. These correlations have been selected following the guidelines provided in two well-known handbooks for heat transfer and heat exchanger design, i.e., Shah and Sekulić [20] and VDI e. V. [24]. The correlations are formulated in non-dimensional terms, i.e., Colburn factor j or Nusselt number for the heat transfer coefficient, and friction factor f for the pressure drop. Tables 1 and 2 list the set of correlations implemented in the HEXs models, for both the refrigerant and the air side. Notice that the correlation

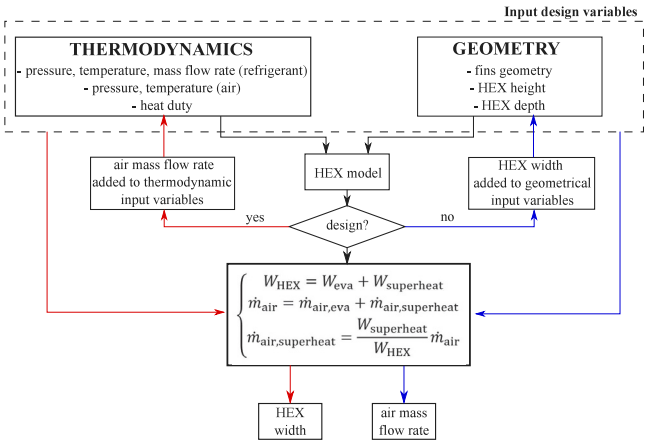

Fig. 4. Flow chart illustrating the on/off-design calculation methodology used for the HEXs (exemplary case: evaporator).

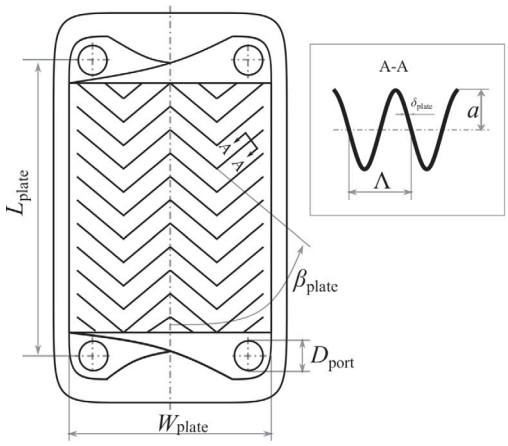

Fig. 5. Chevron-type plate heat exchanger geometry.

by Kim and Bullard [25] has been preferred to that of Chang and Wang [26] to predict the friction factor on the air side of the HEXs, as it accounts also for the effect of the fin depth. Moreover, regarding the prediction of the two-phase flow friction factor inside the flat tubes, the correlation by Schmidt et al. [23] has been selected in place of those proposed by Lockhart and Martinelli [27] and Chisholm [28], given its independence from the range of the mass flux G. Finally, the overall heat transfer coefficient (U) also accounts for the wall thermal resistance, according to the method described by Yadav et al. [29]. In each control volume, the heat transfer rate is estimated according to the relation between the effectiveness (ϵ) and the number of thermal units (NTU) of the heat exchanger. The material assumed for both the condenser and the evaporator is the 3003 Aluminum alloy.

The flow chart in Fig. 4 shows the computational scheme, depending on the type of calculation, thus either an on- or off-design calculation. More specifically, in *on-design* mode, the operating conditions at the inlet and outlet of the HEXs are provided as input values, and the main dimensions are estimated (e.g., the HEX width) to match the required thermal load. In *off-design* mode, the geometry is fully specified, while one of the thermodynamic input variables (e.g., the air mass flow rate) is calculated.

3.1.2. Intercooler

The other heat exchanger of the system is the intercooler, or economizer. It consists of a chevron gasketed Plate Heat Exchanger (PHEX). A number of gasketed metal plates of rectangular shape are clamped together. A corrugated surface is stamped on each thin plate to create interconnected parallel flow channels where the refrigerant flows with multiple changes in direction. The chevron-type corrugation, in particular, features a sinusoidal pattern, whose crests and troughs are oriented with a certain angle against the main flow direction in one or several strips of fixed width, as shown in Fig. 5 [35].

At each corner of the plates, there are circular ports where the refrigerant enters the HEX to be directed through the channels formed in the space between two plates, before exiting. PHEXs operate at moderate temperature and pressure. They are typically employed for liquid-to-liquid or liquid-to-two phase heat transfer and their compactness factor ranges from 120 to 230 m^2/m^3 [18]. For the selected application, the refrigerant is liquid on one side and two-phase on the other side. The model is zero-dimensional and, depending on the refrigerant phase, different correlations have been implemented in the code to estimate the heat transfer coefficient and the pressure drop, as listed in Table 3. This set of equations has been chosen according to the recommendations by Palm and Claesson [36]. Also in this case, the effectiveness-NTU method is used to calculate the heat duty. The geometrical characterization of the PHEX follows the procedure described by Shah and Sekulić [20]. The model has been verified by comparing the results with those obtained using a well-established commercial software for HEX design [37]. The comparison shows a 2% deviation in the calculation of the heat transfer surface and a deviation of less than 1% in the computation of the outlet flow temperature. A discrepancy lower than 15% is obtained for the non-dimensional numbers characterizing both flow streams, i.e., Re and Pr. The heat transfer coefficient of the single-phase and of the two-phase refrigerant flows are estimated with an uncertainty approximately equal to 18% and 5%, respectively.

3.2. Centrifugal compressor

The recent development of high-speed permanent-magnet electric motors technology has stimulated research in the field of small-scale centrifugal compressors, which feature many advantages if compared to larger and heavier positive displacement machines. For example, high-speed radial compressors are an attractive solution as components of refrigeration and heat pump systems, air management systems of fuel cells, electric superchargers for automotive, and fuel delivery systems [40]. According to the same authors, small-scale radial compressors can reach high efficiency (up to 85%) and can be reliable and durable due to the absence of sliding surfaces and complex kinematics. Moreover, the use of foil or magnetic bearings eliminates the need for a lubrication system, which is particularly attractive for refrigeration and heat pump systems, as it avoids all the problems associated with the presence of oil within the system, and, in particular, in the evaporator whose aerothermal efficiency is negatively affected by oil accumulation within its tubes [41]. Finally, the comparatively small dimensions of these compressors mean also that they are inherently light (the total weight is mostly dependent on the weight of the casing and of the electric motor). All these features make high-speed centrifugal compressors particularly suitable for VCC systems for aircraft ECS.

The work presented here is part of a project involving the development of a twin-stage back-to-back centrifugal compressor for large rotorcraft ECS in which its impact on system COP and weight will also be quantified. The simplified design methodology integrated into the system design method presented here is based on the guidelines documented in [42] and makes use of a mean-line code to predict the fluid-dynamic design and performance of the compressor at design point. The model does not account for the pressure recovery due to the volute and the exit cone.

The compressor design model relies on a set of design variables, namely: working fluid, mass flow rate, total inlet pressure and temperature, swallowing capacity (Φ_t), isentropic loading coefficient (Ψ), shape

Table 1
List of empirical correlations selected for the condenser and evaporator heat transfer coefficient estimation.

Heat transfer		
Working fluid	Reference	Equation
Air	Chang and Wang [26]	$j = Re_{Lp}^{-0.487}\left(\frac{\Theta}{90}\right)^{0.257}\left(\frac{F_p}{L_p}\right)^{-0.13}\left(\frac{b}{L_p}\right)^{-0.29}\left(\frac{F_d}{L_p}\right)^{-0.235}\times \left(\frac{L_l}{L_p}\right)^{0.68}\left(\frac{T_p}{L_p}\right)^{-0.279}\left(\frac{\delta_f}{L_p}\right)^{-0.05}$
Single-phase refrigerant	Gnielinski [30]	$\bullet\begin{cases} Nu = \left\{4.364^3 + \left(1.953\sqrt[3]{RePrD_i/l} - 1\right)^3 + \left(0.924\sqrt[3]{Pr}\sqrt{Re(D_i/l)}\right)^3\right\}^{1/3}, \\ Re < 2300 \end{cases}$
		$\bullet\begin{cases} Nu = 0.0214(Re^{0.8} - 100)Pr^{0.4}[1 + (D_i/l)^{2/3}], \\ 0.5 \le Pr \le 1.5; 2300 \le Re \le 10^4 \end{cases}$
		$\bullet\begin{cases} Nu = 0.012(Re^{0.87} - 280)Pr^{0.4}[1 + (D_i/l)^{2/3}], \\ 1.5 \le Pr \le 500; 2300 \le Re \le 10^4 \end{cases}$
		$\bullet\begin{cases} Nu = \dfrac{(\xi/8)RePr}{1 + 12.7\sqrt{(\xi/8)}(Pr^{2/3} - 1)}[1 + (D_i/l)^{2/3}], \\ \xi = (1.8\log_{10} Re - 1.5)^{-2}, \\ Re > 10^4 \end{cases}$
Evaporation	Kandlikar [31]	$\begin{cases} h = h_L[C_1 Co^{C_2}(25Fr_L)^{C_5} + C_3 Bo^{C4}F_{fl}], \\ h_L = 0.023 Re_L^{0.8} Pr_L^{0.4}(k_L/D_i) \end{cases}$
Condensation	Shah [32]	$h = 0.023\frac{k_L}{D_i}Re_L^{0.8}Pr_L^{0.4}\left\{(1-x)^{0.8} + \frac{3.8x^{0.76}(1-x)^{0.04}}{(p_{sat}/p_{cr})^{0.38}}\right\}$

Table 2
List of empirical correlations selected for the friction factor estimation of condenser and evaporator.

Pressure drop		
Working fluid	Reference	Equation
Air	Kim and Bullard [25]	$f = Re_{Lp}^{-0.487}\left(\frac{\Theta}{90}\right)^{0.444}\left(\frac{F_p}{L_p}\right)^{-1.682}\left(\frac{b}{L_p}\right)^{-1.22}\left(\frac{F_d}{L_p}\right)^{0.818}\left(\frac{L_l}{L_p}\right)^{1.97}$
Single phase refrigerant	Kast et al. [33]	$\bullet f = \frac{64}{Re},\ Re < 3000$
		$\bullet f = \frac{0.3164}{\sqrt[4]{Re}},\ 3000 \le Re \le 10^4$
		$\bullet f = 0.0054 + \frac{0.3964}{Re^{0.3}},\ 2\cdot 10^4 \le Re \le 2\cdot 10^6$
		$\bullet \frac{1}{\sqrt{f}} = -0.8 + 2\log(Re\sqrt{f}),\ Re > 10^6$
Two-phase refrigerant	Schmidt and Friedel [34]	$\begin{cases} \left(\frac{\Delta p}{l}\right) = \Phi_L^2\left(\frac{\Delta p}{l}\right)_L, \\ \Phi_L^2 = E + \frac{3.24FH}{Fr^{0.045}We^{0.035}}, \\ E = (1-x)^2 + x^2(f_V/f_L)(\rho_L/\rho_V), \\ F = x^{0.78}(1-x)^{0.24}, \\ H = (\rho_L/\rho_V)^{0.91}(\mu_V/\mu_L)^{0.19}(1-\mu_V/\mu_L)^{0.7} \end{cases}$

Table 3
List of empirical correlations selected for the aerothermal characterization of the chevron gasketed PHEX.

Heat transfer		
Working fluid	Reference	Equation
Single-phase refrigerant	Martin [38]	$Nu = 1.615\left[\left(f\frac{Re}{64}\right)RePr\left(\frac{D_h}{\Lambda}\right)\sin(2\beta_{plate})\right]^{1/3}$
Two-phase refrigerant	Cooper [39]	$h = 55(Pr^{0.12-0.2\log_{10} Ra})(-\log_{10} Pr)^{-0.55}M_r^{-0.5}q^{0.8}$
Pressure drop		
Single-phase refrigerant	Martin [38]	$\begin{cases} \frac{1}{\sqrt{f}} = \frac{\cos\beta_{plate}}{\sqrt{0.18\tan\beta_{plate} + 0.36\sin\beta_{plate} + f_0(Re)/\cos\beta_{plate}}} + \frac{1-\cos\beta_{plate}}{\sqrt{f_1(Re)}}, \\ f_0(Re) = 64/Re,\ Re < 2000 \\ f_0(Re) = (1.8\ln Re - 1.5)^{-2},\ Re \ge 2000 \\ f_1(Re) = 3.8(597/Re) + 3.85,\ Re < 2000 \\ f_1(Re) = 3.8(39/Re^{0.289}),\ Re \ge 2000 \end{cases}$
Two-phase refrigerant	Lockhart and Martinelli [27]	$\begin{cases} \left(\frac{\Delta p}{l}\right) = \phi_L^2\left(\frac{\Delta p}{l}\right)_L, \\ \phi_L^2 = 1 + \frac{K}{X} + \frac{1}{X^2}, \\ X = \left(\frac{1-x}{x}\right)^{(2-n)/2}\left(\frac{\mu_L}{\mu_V}\right)^{n/2}\left(\frac{\rho_V}{\rho_L}\right)^{0.5} \end{cases}$

Table 4
List of semi-empirical correlations selected for the estimation of the impeller losses in the centrifugal compressor model.

Internal losses	
Loss mechanism	Loss model
Blade loading	Coppage and Dallenbach [46]
Skin friction	Jansen [47]
Clearance	Jansen [47]
Mixing	Johnston and Dean [48]

External losses	
Loss mechanism	Loss model
Disc friction	Daily and Nece [49]
Recirculation	Oh et al. [45]
Leakage	Aungier [50]

factor (k), impeller outlet absolute angle (α_2), number of blades (N_{bl}) and diffuser pressure recovery factor (C_p). Assuming no inlet guide vanes, the flow is taken as uniform at the impeller inlet section. The design of the impeller inlet geometry follows the approach proposed by Rusch and Casey [43]. Their work illustrates a design methodology for high-loaded radial compressors, accounting for the requirements of high efficiency and compactness. The aforementioned swallowing capacity is a non-dimensional parameter proportional to the compressor flow coefficient, and is defined as

$$\Phi_t = \frac{\dot{m}}{\rho_{tot,1} D_2^2 u_2} = \frac{\dot{V}_1}{D_2^3 \Omega} \tag{1}$$

The design of highly loaded centrifugal compressors with large swallowing capacity must account for limitations on the maximum inlet relative Mach number at the shroud. In particular, Mach number higher than ≈ 1.35 may trigger boundary layer separation due to shock interaction within the rotor flow channels, causing additional losses associated with secondary flow and mixing. To account for this effect, Rusch and Casey [43] have defined a modified mass flow Φ'

$$\Phi' = \Phi_t \frac{4M_{u_2}^2}{k\pi} = \frac{M_{w_{1,s}}^3 \sin^2\beta_{1,s}\cos\beta_{1,s}}{\left(1 + \frac{\gamma_{Pv}-1}{2} M_{w_{1,s}}^2 \cos^2\beta_{1,s}\right)^{1/(\gamma_{Pv}-1)+3/2}}, \tag{2}$$

which is thus a function of the inlet blade metal angle at the impeller inlet casing ($\beta_{1,s}$) and of the relative inlet Mach number at the shroud ($M_{w_{1,s}}$). The authors demonstrate that, for a given Φ', it is possible to univocally determine the $\beta_{1,s}$ which minimizes $M_{w_{1,s}}$. Hence, to reduce the effect of shock losses, an optimal inlet blade metal angle corresponding to the lowest impeller inlet relative Mach number can be defined for each design point as

$$\cos\beta_{1s,opt} = \frac{\sqrt{3+\gamma_{Pv} M_{w_{1,s}}^2 + 2M_{w_{1,s}}} - \sqrt{3+\gamma_{Pv} M_{w_{1,s}}^2 - 2M_{w_{1,s}}}}{2M_{w_{1,s}}}. \tag{3}$$

Given this information, the static thermodynamic state and the velocity triangle at the inlet of the impeller can be obtained. The meanline model considers the effect of the slip at the impeller outlet to estimate the velocity triangle by accounting for the flow angular momentum reduction. The slip factor, calculated using the model proposed by von Backström [44], quantifies the deviation of the outlet relative flow angle from the impeller outlet blade metal angle.

The impeller efficiency is estimated by means of a set of semi-empirical loss correlations indicated by Oh et al. [45] (Table 4). Four internal loss mechanisms, namely blade loading, clearance, mixing and friction losses, have been considered to estimate the actual flow total pressure rise. Incidence and shock losses are neglected in on-design simulations. External parasitic losses, i.e., recirculation, disc friction and leakage, are taken into account for the estimation of the total-to-total efficiency.

Downstream of the impeller, a vaneless diffuser with parallel walls is considered. The design of the diffuser only accounts for the skin friction losses along the channel, according to the model proposed by De Bellis et al. [51]. The model is based on a non-iterative approach, simplifying the classical set of conservation equations described by Stanitz [52]. The diffuser is assumed of constant width d, and the effect of blade wakes and aerodynamic blockage are neglected. The angular momentum equation accounts for fluid-dynamic losses associated with friction. The loss of angular momentum is computed by integrating the moment of the elementary friction forces over the two diffuser surfaces. Under the assumption of a constant product of radius and the tangential component of the flow velocity along the diffuser, the pressure losses are considered concentrated at the diffuser outlet. Hence, the equation of the angular momentum per unit of mass can be expressed as

$$D_3 c_{u,3} = D_4 c_{u,4} + \Delta AM = D_4 c_{u,4}\left(1 + \frac{W_f}{c_4 c_3}\right) \tag{4}$$

The dissipative term ΔAM is a simple function of the specific work dissipated due to friction

$$W_f = C_f \frac{(c_3 R_3)^2}{d\cos\alpha_4}\left(\frac{R_4 - R_3}{R_4 R_3}\right), \tag{5}$$

with

$$C_f = \frac{0.5}{Re_x^{0.3}}. \tag{6}$$

The diffuser skin friction coefficient C_f is defined according to Dubitsky and Japikse [53]. It corresponds to an average value which is a function of the Reynolds number Re_x whose characteristic length is estimated assuming that the mean flow path follows a logarithmic spiral trajectory through the diffuser.

The compressor model includes a method for the estimation of the axial thrust, whose maximum value is a design constraint for the bearings. Newton's second law is commonly used for axial thrust calculation, which gives

$$F_{axial} = F_{eye+nose} + F_{shroud} + F_{impulse} - F_{backdisk}. \tag{7}$$

A reliable prediction of the pressure distribution over the shroud and the back disk of the impeller is needed to estimate the various force terms in the equation. The model, therefore, includes the calculation procedure proposed by Tiainen et al. [54], which consists of a set of equations combining different analytical models. More in detail, the force acting on the impeller eye and nose is calculated using the model by Nguyen-Schäfer [55]. The impulse force and the force acting on the shroud are retrieved with the model proposed by Japikse [56]. The back disk force is computed by means of the model by Larjola [57], which is based on the assumption that a fluid element is in radial equilibrium so that the pressure force balances the centrifugal force. Note also that the axial thrust is computed without accounting for the presence of labyrinth seals.

The twin-stage radial compressor features a configuration where the two impellers are mounted back-to-back on the same shaft in order to balance the axial thrust. The two stages rotate therefore with the same speed and, as a consequence, the loading coefficient is an independent variable of the model only for the preliminary design of the second stage of the compressor, while it is as an output for that of the first stage. Finally, the twin-stage centrifugal compressor model also takes into account the electric motor cooling by assuming that the electric motor efficiency is equal to 95% and that all the electromagnetic losses are dissipated as heat. The refrigerant mass flow rate exiting the first stage of the compressor is used to cool the electric motor. The cooling of the bearings is neglected.

Table 5
List of correlations selected for the friction factor estimation in straight pipes [33].

Flow regime	Friction factor	Correlation
Laminar	$f = \frac{64}{Re}, Re < 2300$	Hagen–Poiseuille
Transitional	$f = \frac{0.316}{Re^{0.25}}, 2300 < Re < 4000$	Blasius
Turbulent	$\frac{1}{\sqrt{f}} = -2 - \ln\left(\frac{\epsilon}{3.71D} + \frac{2.51}{Re\sqrt{f}}\right), Re > 4000$	Colebrook and White

The output of the centrifugal compressor model has been verified by comparison with the output of *TurboSim*, a validated in-house tool for turbomachinery design and optimization documented in [42], obtaining a maximum discrepancy of the results equal to 8%.

3.3. Pipeline

The VCC system performance can be significantly affected by the pressure drop due to the working fluid flowing through the pipes of the system, as they are usually quite long. In particular, if the working fluid is a low-density refrigerant enabling the design of a more efficient compressor, the friction losses in the pipeline operating at the lowest temperature level (e.g., the one connected to the evaporator) may become critical. In this regard, the correct sizing of the hoses is fundamental to evaluate the influence of pressure drops in the refrigerant loop on system efficiency. The duct model is zero-dimensional. It can be used either in *on-design mode* to size the pipe internal diameter given the length, surface roughness and thermodynamic conditions, or in *off-design mode* to calculate the pressure drop given the duct dimensions. The friction factor is estimated from the set of correlations listed in Table 5, depending on the flow regime.

The developed ECS model for large helicopters includes several piping model components. In particular, the three longest ducts of the system are taken into account, namely, the hose channelling the refrigerant from the evaporator to the compressor, the duct connecting the compressor outlet to the condenser and the pipe connecting the intercooler and the evaporator inlet. All pipes are assumed to be made of stainless steel (AISI 304).

The pipeline weight is calculated from the tube thickness estimation. The ASME B31.5 [58] provides the relation

$$\delta_{\text{pipe}} = \frac{p_{\text{gauge}} D_{\text{out}}}{2(\sigma_{\max} + p_{\text{gauge}} y)} \tag{8}$$

to calculate the minimum allowable thickness (δ_{pipe}) of straight pipes to withstand the internal design gauge pressure (p_{gauge}). In the case of aerospace applications, specific guidelines are set out for the estimation of the internal design gauge pressure. The CS-25 Amendment 3 [59] advises to account for a multiplication safety factor equal to 3 for the system design pressure.

4. Integrated system design optimization method

An in-house software tool has been developed to allow for the preliminary integrated design optimization of aircraft/helicopter ECS. The tool consists of the interface of an open-source optimization algorithm developed in Python with the executable of the system model generated by a Modelica commercial software [60]. For the application of the method to the helicopter ECS case study, specific component models from the *DeSimECS* library were assembled into a system model which reproduces the ECS configuration reported in the process flow diagram of Fig. 1(a). The optimization design problem is formulated in terms of two conflicting objective functions $f(x)$, namely the system COP and the system weight. More specifically, the weight calculation is only accounting for the system HEXs and the piping, since the weight of the compressor is not expected to change significantly with the system COP, due to the corresponding small variation in the overall size and electric power of the machine. The optimization design problem is restricted by inequality constraints $g_k(x)$. The optimal solution is numerically obtained with a Genetic Algorithm (GA). The associated mathematical problem can be expressed as

$$\begin{aligned} &\min/\max \quad f_q(x), \quad q = 1, \dots, \mathrm{Q} \quad \forall x \in \mathbb{R}, \\ &\text{s.t.} \quad \begin{cases} g_j(x) \le 0, & j = 1, \dots, \mathrm{J} \\ x_n^{(\mathrm{L})} \le x_n \le x_n^{(\mathrm{U})}, & n = 1, \dots, \mathrm{N}. \end{cases} \end{aligned} \tag{9}$$

More specifically, when running the GA, for each generation a matrix $\mathbf{X}_{\mathrm{M\times N}}$ is created to store the vectors of N system design variables for each of the M individuals. These values are provided as input to the Modelica model that is executed at each iteration of the optimization program. The results of the simulations are then stored in an output matrix $\mathbf{Y}_{\mathrm{M\times N}}$. The GA initializes a population of solutions and, through the repetitive application of sampling, crossover, mutation, and evaluation, improves each generation towards the defined objective. This process is iterated until the optimizer convergence criteria are satisfied and the optimal non-dominated solutions of the objective functions are found, see Fig. 6.

Table 6
Operating conditions of the helicopter ECS on the ground (hot and humid day).

Helicopter ECS system for cabin air conditioning		
Refrigerant loop		
Evaporation temperature	$T_{\text{air,env}}$	0 °C
Evaporator cooling duty	$\dot{Q}_{\text{eva}}$	12.5 kW
Air side		
Environmental air temperature	$T_{\text{air,env}}$	40 °C
Recirculated cabin air temperature	$T_{\text{air,rec}}$	28 °C
Ram air mass flow rate	$\dot{m}_{\text{ram}}$	1.1 kg/s
Fresh cabin air mass flow rate	$\dot{m}_{\text{fresh,cb}}$	0.1 kg/s
Recirculated cabin air mass flow rate	$\dot{m}_{\text{rec,cb}}$	0.5 kg/s

4.1. Case study

The integrated preliminary system design optimization method (Section 4) has been tested by applying it to the design of the VCC system of a large passenger helicopter ECS (20 passengers and 2 pilots). The optimization considers a single operating condition: the helicopter is on the ground, during a hot and humid day, thus arguably the most demanding and thus critical condition [15]. The environmental air temperature is set equal to 40 °C with 40% relative humidity, and the cooling duty is 12.5 kW. Table 6 lists all the system specifications.

Both the evaporator and the condenser model are used in *on-design mode*, i.e., the air mass flow rate is set and the HEX width is calculated (HEX design). As far as the evaporator is concerned, the cabin air mass flow rate is prescribed according to the standard ARP292 [15]. For what regards the condenser, the required ram air mass flow rate is approximately equal to 1.1 kg/s, as reported in Ascione et al. [61], hence any change in the air pressure drop across the HEX leads to a variation of the cooling air fan power consumption. The values of the fixed parameters defining the geometry of the louvered fins and the minichannels are listed in Table 7. The multilouvered fins dimensions significantly affect the air heat transfer efficiency, as well as the total weight of the HEX. For this reason, all the fins geometrical parameters are taken as design optimization variables, except for the fins pitch (F_{p}) and the fins thickness (δ_{f}), whose values are limited based on manufacturing considerations [62].

For what regards the intercooler, the plates length is computed while the chevron-plate geometrical parameters (Table 8) and the heat load are design inputs.

The sizing of the piping is performed by prescribing the allowed pressure drop and tube length. The internal hose diameter and the refrigerant velocity are then calculated. This design choice allows for the

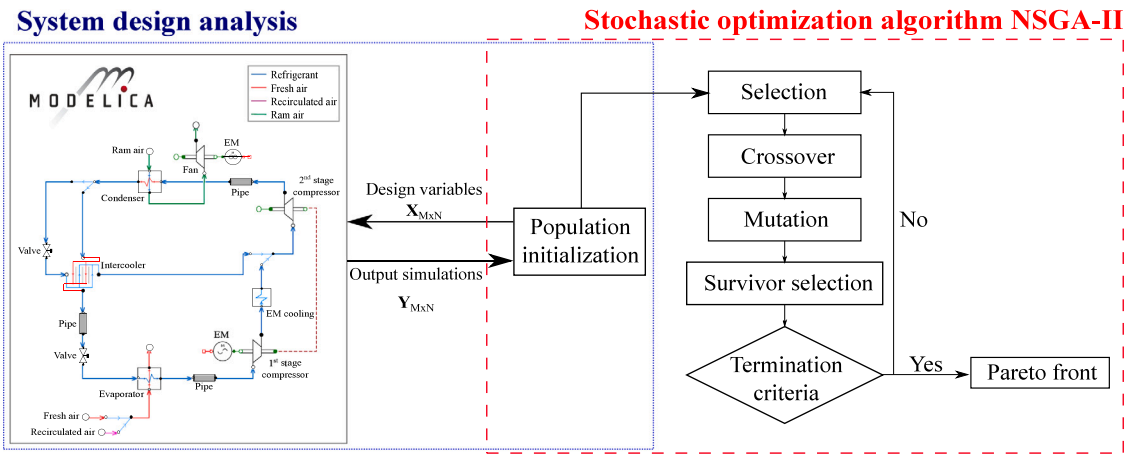

Fig. 6. Flowchart illustrating the integrated system design optimization framework coupling the helicopter ECS Modelica model to the stochastic optimization algorithm.

Table 7
Geometrical parameters of the multi-louvered fins and of the minichannels of the condenser and of the evaporator.

Evaporator		
Geometrical parameter	Symbol	Value
Tube height	T_h	2 mm
Tube wall thickness	δ_t	0.4 mm
Tubes pitch	T_p	9.4 mm
Number of minichannels	N_{mc}	16
Minichannels wall thickness	δ_{mc}	0.35 mm
Fins pitch	F_p	3 mm
Fins thickness	δ_f	0.12 mm

Condenser		
Geometrical parameter	Symbol	Value
Tube height	T_h	1.93 mm
Tube wall thickness	δ_t	0.4 mm
Tubes pitch	T_p	2.33 mm
Number of minichannels	N_{mc}	12
Minichannels wall thickness	δ_{mc}	0.3 mm
Fins pitch	F_p	1.4 mm
Fins thickness	δ_f	0.115 mm

Table 8
Geometrical parameters of the flat plate chevron type HEX used as intercooler.

Intercooler		
Geometrical parameter	Symbol	Value
Number of passes (both refrigerant streams)	N_{pass}	1
Number of channels per pass (both refrigerant streams)	$N_{channel}$	40
Flat plate width	W_{plate}	120 mm
Port diameter	D_{port}	30 mm
Amplitude sinusoidal corrugation pattern	A	1.5 mm
Wave length corrugation pattern	a	10 mm
Flat plate thickness	δ_{plate}	0.4 mm
Plate inclination angle	β_{plate}	60°

analysis of the working fluid influence on the piping size and weight. The pipe thickness is estimated by assuming that the saturation pressure at 80 °C is the design gauge pressure. 80 °C is the highest temperature the refrigerant loop can reach when the helicopter is on the ground and the VCC system is not in operation. Since the error associated with the hoses weight estimation is inherently small with respect to the entire system, only three main piping lines are considered in this study: the hose connecting the evaporator outlet to the compressor suction side, the one between the compressor outlet and the condenser inlet, and the one between the intercooler and the throttling valve. The length of each line is assumed to be equal to 4 m, 1 m, and 2 m, respectively.

4.2. Design space and constraints

The weight function is evaluated by summing the weight of the three HEXs, which is further increased by 25% to account for the weight of the brazed junctions and of the mixing manifolds, to the weight of the piping. The weight of the compressor and of other minor auxiliaries is neglected as it is expected not to change appreciably with the working fluid characteristics and the selected design variables of the system. The calculated optimal weight is therefore lower than the actual total weight. The system efficiency is defined as the ratio between the evaporator thermal power required for the cabin cooling and the sum of electric power needed by the ram air fan and by the twin-stage centrifugal compressor, namely as

$$\mathrm{COP} = \frac{\dot{Q}_{eva}}{\dot{W}_{compr} + \dot{W}_{fan}}. \tag{10}$$

The mixed-integer constrained optimization problem is defined by 24 design variables, whereby the impellers' number of blades is the only integer value. The problem is subjected to 26 inequality constraints. Among those, the geometrical parameters are limited due to practical considerations related to manufacturability and material mechanical strength. The initial population consists of 10 individuals for each design variable, for a total of 240 individuals. The initial points are sampled differently according to the variable type, i.e., with random sampling for integers, and with the Latin hypercube approach for the real number variables. The Non-Sorted Genetic Algorithm-II (NSGA-II) implemented in the open-source Pymoo library [63] has been selected to perform the numerical optimization. Table 9 lists the design variables and the value of the constraints chosen for this case study. The convergence was reached after 240 generations, corresponding to a total of 57,600 function evaluations. Once the optimal set of non-dominated solutions of the two objective functions is found, the analysis of the optimal design of all the system main components, namely heat exchangers, centrifugal compressor and piping, can be performed.

Table 9
Design variables and constraints values selected for the design optimization case study.

Design variables			
Variable	Symbol	Min. value	Max. value
Intermediate pressure	p_{int} [bar]	6	10
Condensation temperature	T_{cond} [°C]	45	75
ΔT at pinch point (intercooler)	$\Delta T_{pp,int}$ [K]	5	15
Louver angle (evap. and cond.)	Θ [°]	25	35
Louver pitch (evap. and cond.)	L_p [mm]	0.50	3
Louver length (evap. and cond.)	L_l [mm]	2.13	18.5
HEX height (evap. and cond.)	H_{HEX} [mm]	100	500
Evaporator depth	D_{eva} [mm]	20	60
Condenser depth	D_{cond} [mm]	10	60
Swallowing capacity (1st, 2nd stage)	Φ_{t1} [–]	0.02	0.20
Shape factor (1st, 2nd stage)	k [–]	0.65	0.90
Absolute outlet angle (1st, 2nd stage)	α_2 [°]	60	75
Number of blades (1st, 2nd stage)	N_{bl} [–]	10	20
Diffuser pressure recovery factor (1st, 2nd stage)	C_p [–]	0.45	0.65
Loading coefficient (2nd stage)	Ψ [–]	0.65	1

Constraints values			
Variable	Symbol	Min. value	Max. value
HEX width (evap. and cond.)	W_{HEX} [mm]	50	800
Refrigerant velocity (evap. and cond.)	v_{refr} [m/s]	–	20
Air velocity (evap. and cond.)	v_{air} [m/s]	–	20
ΔT at pinch point (condenser)	$\Delta T_{pp,cond}$ [K]	5	20
Refrigerant pressure drop (evap. and cond.)	Δp_{refr} [bar]	–	0.8
Air pressure drop (evap. and cond.)	Δp_{air} [Pa]	–	400
Inlet hub radius (1st, 2nd stage)	$R_{1,hub}$ [mm]	2.5	–
Outlet blade height (1st, 2nd stage)	$H_{2,blade}$ [mm]	0.8	–
Outlet relative blade angle (1st, 2nd stage)	$\beta_{2,blade}$ [°]	−45	−10
Rotational speed (1st, 2nd stage)	Ω [krpm]	10	200
Inlet relative Mach at shroud (1st, 2nd stage)	$M_{w_{1,s}}$ [–]	–	0.98
Outlet absolute Mach (1st, 2nd stage)	M_2 [–]	–	0.98
Outlet relative Mach at shroud (1st, 2nd stage)	$M_{w_{2,s}}$ [–]	–	0.98
Net axial thrust twin-stage compr.	F_{axial} [N]	0	26

5. Results and discussion

The outcome of the integrated system design optimization is a set of solutions lying on a Pareto frontier. Fig. 7 shows the set of non-dominated solutions as a function of the two conflicting objectives.

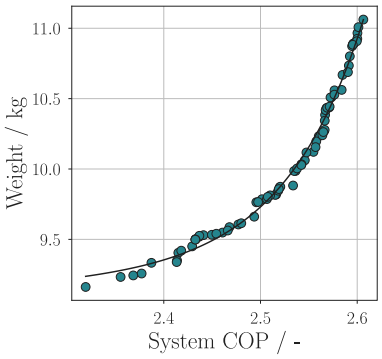

Fig. 7. Pareto frontier (—) and set of non-dominated solutions (●) resulting from the integrated system design method applied to the multi-objective optimization of the ECS. The weight is not the total weight of the system, as only the weight of HEXs and main piping is considered (the components whose weight is directly linked to the system efficiency).

For the considered operating condition, the sizing of the condenser is the most critical in comparison to the sizing of the other HEXs (Fig. 8(a)). This can be reasoned considering that, for a constant ram air mass flow rate through the condenser, the larger the HEX, the lower the associated friction loss and thus the lower the required fan power (Fig. 8(b)), which in turn benefits the system efficiency.

According to Eq. (10), the COP is inversely proportional to the power needed to drive all the turbomachinery. Fig. 8(c) shows that the centrifugal compressor power decreases almost linearly with increasing COP until it reaches a *plateau*. Since the evaporation pressure is a fixed value and the optimal intermediate pressure is approximately equal to 8 bar, this trend only depends on the condensation pressure, whose value decreases for increasing COP until the optimal value of 16.9 bar is reached, which corresponds to a saturation temperature of 60.3 °C. Finally, it can be concluded that any change in the total power required by the centrifugal compressor is principally affected by the design of the high-pressure stage, whose total-to-total compression ratio is a variable dependent on the system efficiency.

5.1. Heat exchangers design

Fig. 9 shows the variation of the three condenser core dimensions, namely the width (Fig. 9(a)), the height (Fig. 9(b)) and the depth (Fig. 9(c)) with the corresponding system weight.

An increase in the system COP is due to a reduction of the ram air pressure drop, which comes at the expense of a larger condenser unit. The optimal condenser design features a small depth and a wide air-side frontal area. The condenser depth is approximately equal to 10 mm, corresponding to the lowest value of the range selected for this design variable. The HEX width, namely the flat tube length, varies between 700 mm and 800 mm. Fig. 9 shows that, among the three HEX core dimensions, only the height is related to the system weight according to an identifiable trend. The variation of the ram air pressure drop is also influenced by the fins geometry. Fig. 10 displays that both larger louver length (Fig. 10(a)) and louver pitch (Fig. 10(b)) guarantee a more uniform flow path, limiting the associated pressure drop. Notably,

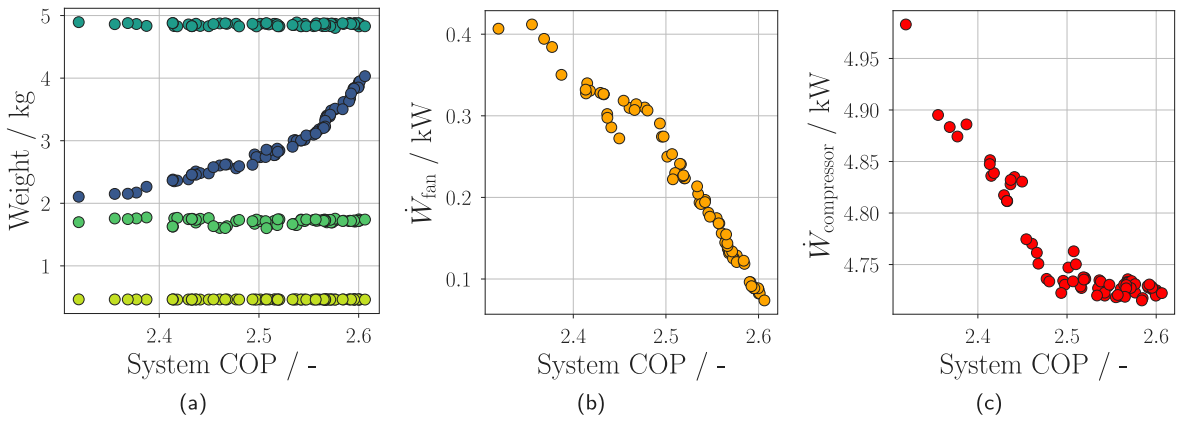

Fig. 8. (a) Breakdown of the system components weight and its effect on the system COP: condenser (●), evaporator (●), intercooler (●), piping (●). Influence of the power requirement of both the ram air fan (●) (b) and the centrifugal compressor (●) (c) on the system COP.

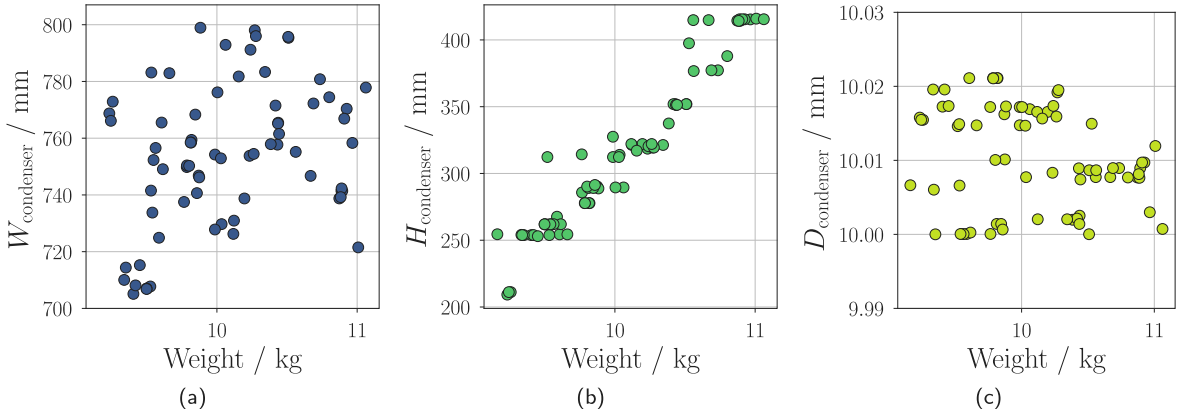

Fig. 9. Condenser core dimensions as a function of the system weight: (a) width (●), (b) height (●), (c) depth (●).

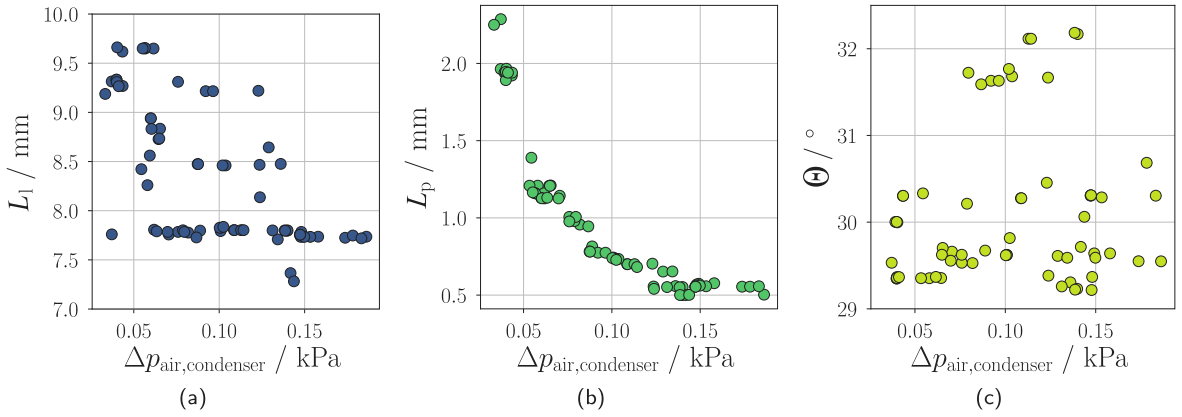

Fig. 10. Condenser fin parameters as a function of the pressure drop associated to the ram air flow: (a) louver length (●), (b) louver pitch (●), (c) louver angle (●).

the louver angle does not significantly affect the fins design, and its optimal value is approximately equal to 30° (Fig. 10(c)).

On the refrigerant side, both the flat tube height and the number of minichannels are fixed. Any increase in the condenser core height corresponds to a larger number of flat tubes, and a consequent reduction of the working fluid velocity. Nonetheless, the refrigerant pressure drop reduction is not significant, since the length of the flat tubes, thus the condenser width, does not vary significantly in the optimal solution set. It is, therefore, possible to conclude that the optimal design features the minimal pressure drop associated with the air flow (Fig. 11(a)), rather than that associated with the refrigerant (Fig. 11(b)), given that the ram air pressure drop directly and considerably affects the fan power consumption, which is inversely proportional to the system COP. The impact of the refrigerant pressure drop on the COP value is lower.

The evaporator design relies on the assumption of constant cooling duty and cabin air mass flow rate. The system optimization leads to the reduction of the pressure losses associated with the refrigerant flow, directly affecting the system COP value. The optimal evaporator design (Fig. 12) is characterized by a core width approximately equal to 795 mm (maximum value, Table 9), a height of 500 mm (minimum value, Table 9), and a depth of 20 mm (minimum value, Table 9).

The fins geometry is characterized by a small louver length (≈ 2.1 mm) and louver pitch (≈ 0.5 mm), and by large louver angles (≈ 35°). Short and oblique fins, with a small louver pitch, enhance the air flow

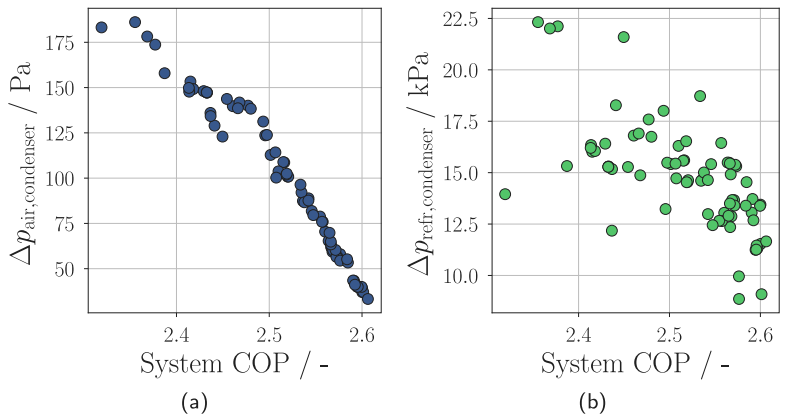

Fig. 11. Pressure drop occurring in the condenser on both ram air (●) (a) and refrigerant side (●) (b) as function of the system COP.

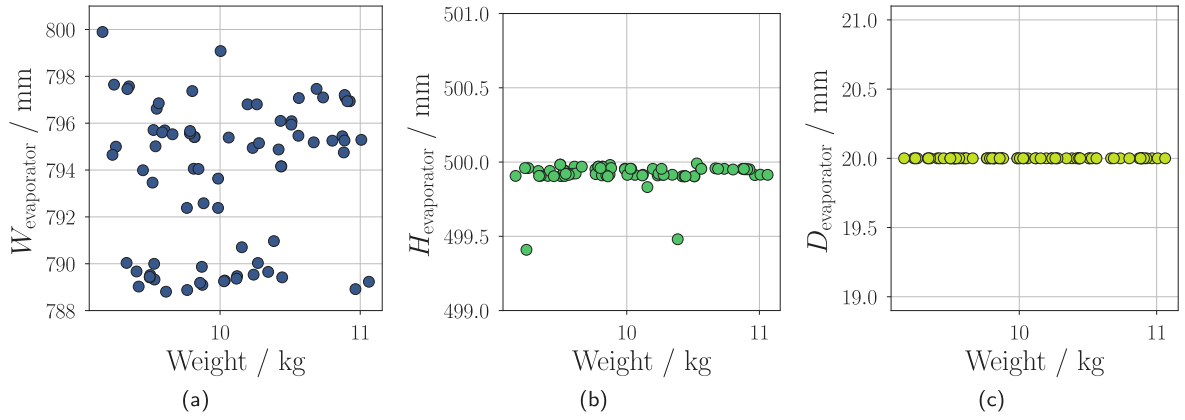

Fig. 12. Evaporator core dimensions as a function of the system weight: (a) width (●), (b) height (●), (c) depth (●).

mixing to achieve the heat transfer coefficient necessary to comply with the target evaporator cooling capacity. The pressure drop for both the refrigerant and the air side does not display any accountable dependence on the system COP.

Finally, for the design of the intercooler the plate length (L_{plate}) is taken as an unknown variable; the geometry is always fixed. The intercooler heat load varies within a small range, whereby the optimal value is equal to 2.9 kW which is achieved in correspondence with the highest system COP values. Consequently, the plate length does not display an identifiable relationship with the objective functions.

5.2. Twin-stage centrifugal compressor design

The optimal centrifugal compressor designs feature a small decrease of the total-to-total compression ratio of both stages as function of the system efficiency. Thus, the optimal compression ratio of the first and the second stage can be averaged respectively to 2.9 and 2.2. To limit the overall computational costs, the centrifugal compressor model does not account for the volute and the exit cone. Hence, the results overestimate the power consumption of the compressor. The two stages are mounted in a back-to-back configuration, and they rotate on a common shaft at a speed that ranges between 195 krpm and 200 krpm. The values of net axial thrust never exceed 5 N. The design of the twin-stage centrifugal compressor is based on a set of input parameters. In correspondence with the optimal solutions on the Pareto frontier, these parameters do not show any analytical dependence on the objective functions. Hence, a set of optimal values for both the first and the second stage can be defined for the system study, and they are listed in Table 10.

The swallowing capacity of the first stage is higher than that of the second stage. The refrigerant mass flow rate is equal to 0.08 kg/s for the first stage, and to 0.10 kg/s for the second stage. However, the effect of vapour compression results in a lower inlet flow density, hence larger volumetric flow rate, at the inlet of the first stage compared to that of the second stage. Accordingly, see also Eq. (1), the size of the impeller of the first stage is larger than that of the second.

Table 10
Set of optimal design input parameters for the twin-stage centrifugal compressor.

Parameter	Symbol	1st stage	2nd stage
Swallowing capacity	Φ_{t1}	0.073	0.068
Loading coefficient	Ψ	0.65	0.80
Shape factor	k	0.80	0.70
Number of blades	N_{bl}	15	20
Inlet absolute flow angle	α_2	70°	73°
Diffuser pressure recovery factor	C_p	0.65	0.65

The trend of the work coefficient is opposite to that of the swallowing capacity: the second stage features higher values than the first stage. The work coefficient is defined as in Eq. (11):

$$\Psi = \frac{\Delta h_{tot}}{(\Omega R_2)^2} \tag{11}$$

The first compressor stage fulfils a total-to-total compression ratio larger than the one of the second stage. For a constant rotational speed, the large impeller outlet diameters of the first stage justify the results obtained for the loading coefficient.

Due to the lower volumetric flow rates at both the inlet and outlet sections, the second stage features flow passages that are smaller than those of the first stage. Fig. 13 shows the trend of the main dimensions of the stage geometries as a function of the system efficiency.

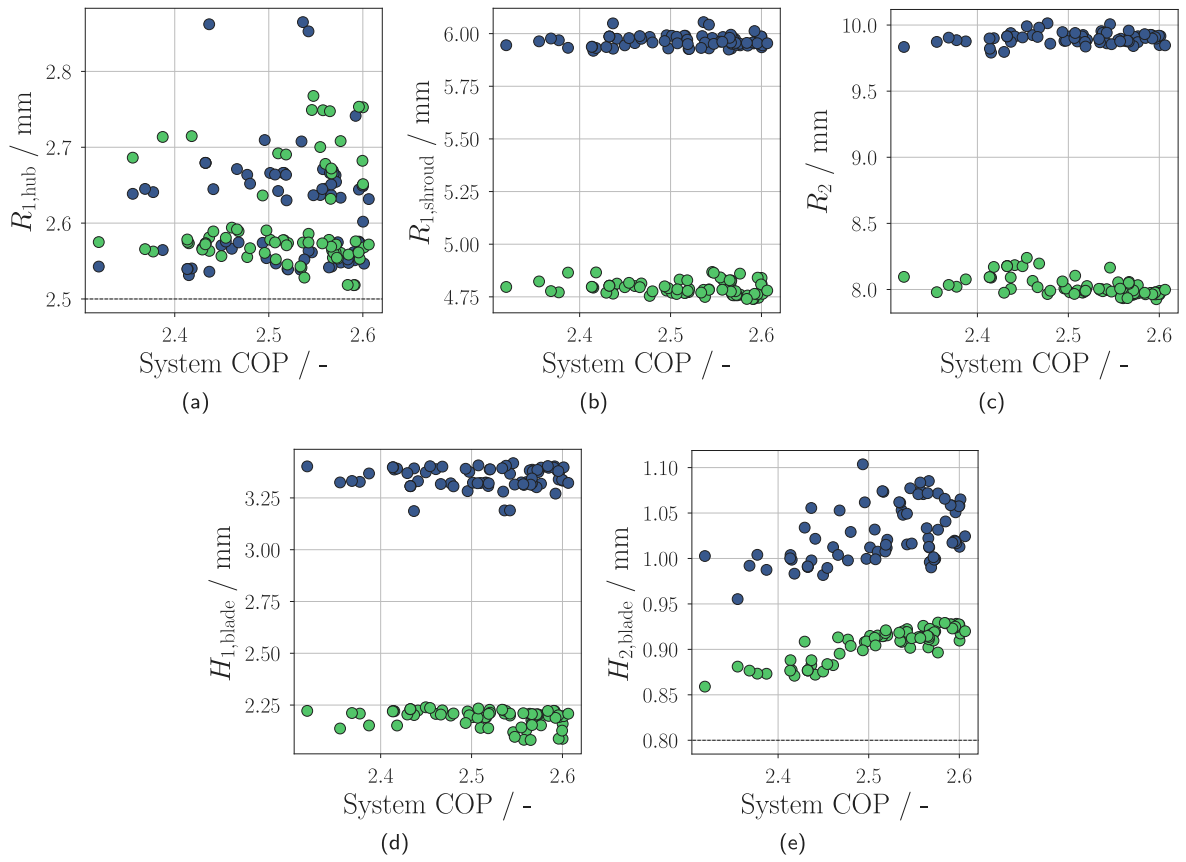

Fig. 13. Geometrical parameters of the impellers of the twin-stage centrifugal compressor (first stage compressor (●) and second stage compressor (●)) as a function of the system COP: (a) inlet radius at the hub, (b) inlet radius at shroud, (c) outlet radius, (d) inlet blade height, (e) outlet blade height.

The second stage design is the most critical, because of its smaller dimensions.

In particular, the impeller radii as well as the inlet blade angle do not show a dependence on the system COP. The inlet optimal hub radius is about 2.6 mm, close to the assumed manufacturability limit (2.5 mm). The optimal inlet radius at the shroud and the outlet impeller radius are equal to 4.8 mm and 8 mm, respectively. Consequently, the inlet blade height, defined as the difference between the inlet radius at the shroud and the one at the hub, does not vary and its optimum corresponds approximately to 2.2 mm. The outlet blade height of the second stage of the compressor is the only dimension showcasing a trend with respect to the system efficiency, whereby higher system efficiency is obtained with higher blades. This trend is due to the decrease of the second stage outlet pressure, namely the system condensation pressure, which corresponds to an increase in stage efficiency. With the decrease of the compression ratio of the second stage, the outlet flow density reduces and this leads to larger volumetric flow rate and flow passages. The same observation is not valid for the first compressor stage, whose outlet blade optimal height does not show a meaningful dependence from the COP, since the optimizer always selects similar values for the outlet pressure, i.e., the system intermediate pressure.

The optimal centrifugal compressor designs feature a small increase of the total-to-total efficiency of both stages with the system COP, as predictable from the trend of the compression ratio. The total-to-total efficiency of the second stage is higher than that of the first stage, with a discrepancy between the two stages equal to 1.5%. Fig. 14 shows the percentage impact of each loss mechanism on the specific work of each stage, calculated as average of the results obtained for all the optimal compressor designs over the Pareto frontier. The two stages have the same rotational speed and the absolute tip clearance is constant for both stages and equal to 0.30 mm. Despite the second stage featuring a smaller outlet blade height as to the first stage, the discrepancy in tip clearance losses between the two stages is not significant thanks to the effect of the lower pressure ratio of the second stage. Globally, the internal losses are almost equal for both stages, while the external losses are significantly larger for the second stage. However, the difference in total-to-total efficiency between the two stages is not remarkable, since the friction losses occurring in the first stage, especially those in the diffuser, compensate for the preponderance of the external losses in the second stage.

6. Sensitivity analysis

A sensitivity analysis study has been carried out to target a subset of design variables which most significantly affect the objective functions, and eventually, reduce the design space of the optimization problem, hence the associated computational cost. The analysis is based on the One-Variable-At-a-Time (OVAT) approach. It consists of the computation of the objective functions by varying the value of a single design variable at the time while keeping the others at their nominal value. The same procedure is repeated for all the design variables independently. The sensitivity is the percentage variation of the objective functions with respect to any change in each one of the design variables. However, the OVAT approach does not account for the interdependence of the model input variables and for the non-linearity of the solution with respect to the design variables. To overcome these limitations, a global sensitivity analysis, i.e., Sobol's method [64], should be selected. This is a probability-based approach for the estimation of the variance of the objective functions attributed to each design variable independently and to their interaction. The drawback of such a methodology is that the number of model runs, needed for the analysis of the probability distributions, grows exponentially with the number

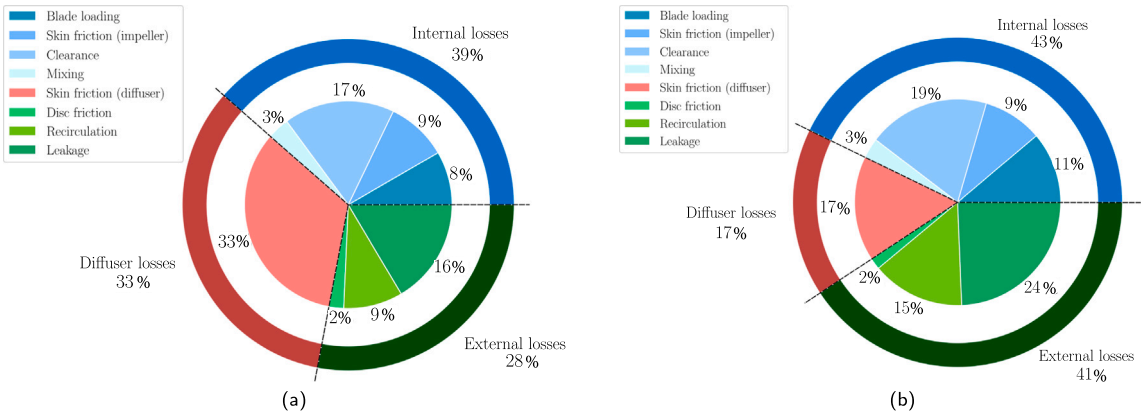

Fig. 14. Twin-stage centrifugal compressor: losses breakdown. (a) First compressor stage, (b) second compressor stage.

of design variables. In the current work, the OVAT approach has been preferred to perform a simplified sensitivity analysis and to overcome the limitations associated with the high computational cost due to the large number of design variables. In the current study, twelve non-dominated solutions from the Pareto frontier have been selected, and the method described before has been applied to the design variable vector associated with each solution. The nominal value of each design variable has been varied within a range of ±10%. The sensitivity of the objective functions to each one of the design variables is computed as an average of the one obtained for all the selected 12 non-dominated solutions. Figs. 15 and 16 show the outcome of the sensitivity analysis for the COP and the system weight, respectively.

Considering a threshold equal to ±1% for the sensitivity of the objective functions, it can be observed that, the system efficiency is strongly dependent on any change in the design variables of both compressor stages, and the intermediate pressure (p_{int}). More specifically, among all the twin-stage centrifugal compressor design variables, the solution is more sensitive to variations of the outlet absolute flow angle (α_2), the diffuser pressure recovery factor (C_p) and the isentropic loading coefficient (λ_{is}), since they directly affect the compressor power requirement. It is interesting to notice that any change in the evaporator design variables does not have any effect on the prediction of the system COP. The opposite occurs for the condenser, whose design is directly correlated to the ram air fan power demand and the condensation temperature (T_{cond}), hence to the system efficiency.

The system weight is only sensitive to the HEXs geometrical design parameters, together with the intermediate pressure (p_{int}) and the condensation temperature (T_{cond}). In particular, the design of the evaporator can affect significantly the solution, hence the selection of the most appropriate range for its design variables is important for a realistic system design.

Finally, the study shows that any change in the number of blades (N_{bl}) of the impeller of both compressor stages, provided that a good estimate is given, the shape factor of the second stage of the compressor (k_{S2}), the pinch-point temperature difference of the intercooler ($\Delta T_{\mathrm{pp,intcool}}$) and the condenser louver length ($L_{\mathrm{l,cond}}$) has no impact on both the objective functions. Consequently, not accounting for the aforementioned variables, the sensitivity analysis identifies a total number of 19 design variables that are significant for the evaluation of the objective functions. The design space associated with the optimization problem may account only for these 19 design variables instead of 24, with a consequent reduction of the computational cost.

7. Conclusions and future work

This article documents a conceptual design method for aircraft/rotorcraft environmental control systems based on a vapour compression cycle powered by a high-speed radial compressor. This method allows the designer to perform the thermodynamic cycle optimization and the preliminary design of the main components simultaneously. The method has been successfully applied to the design of the environmental control system of a large rotorcraft as a study case. The steady-state models of the various system components have been developed using the Modelica acausal modelling language. The design optimization problem is solved using an in-house computer program coupling the Modelica system models to a Python open-source genetic optimization algorithm. A multi-objective constrained system design optimization has been performed for a critical operating condition, i.e., the helicopter being steady on the ground during a hot and humid day.

The main conclusions drawn from this investigation can be summarized as follows:

(i) The proposed method proves that it is possible to optimize complex systems accounting simultaneously for system performance, components design and working fluid.

(ii) The system optimization results in a Pareto front, proving that the system efficiency can be enhanced only at the expense of heavier system components. The condenser sizing is the most critical, since a larger condenser unit reduces the pressure drop associated with the ram air stream and the optimal condensation pressure of the system. Consequently, the total electric power demand of the system decreases in favour of the system efficiency.

(iii) The design of a twin-stage centrifugal compressor to drive the vapour compression cycle of a helicopter environmental control system is feasible. The resulting compressor rotates at very high speed and is quite small. In particular, the high density of the compressed refrigerant vapour entering the second stage makes its design the most challenging due to the small dimensions of the compressor wheel and blade height.

(iv) A realistic optimization of the thermodynamic cycle of the environmental control system must account for the integrated design of the centrifugal compressor. In particular, the design mass flow rate, the compression ratio and the efficiency, resulting from the preliminary design of the turbomachine, have a crucial impact on the system efficiency estimation, as confirmed by the sensitivity analysis. At the same time, the sole optimization of the thermodynamic cycle parameters may lead to unfeasible design specifications for the compressor, given the manufacturing constraints and the small power capacity of the machine.

(v) The sensitivity analysis demonstrates that only 19 design variables have a significant influence on the prediction of the objective functions. Hence, the design space may be narrowed down, with a consequent reduction in the computational cost associated with the optimization problem.

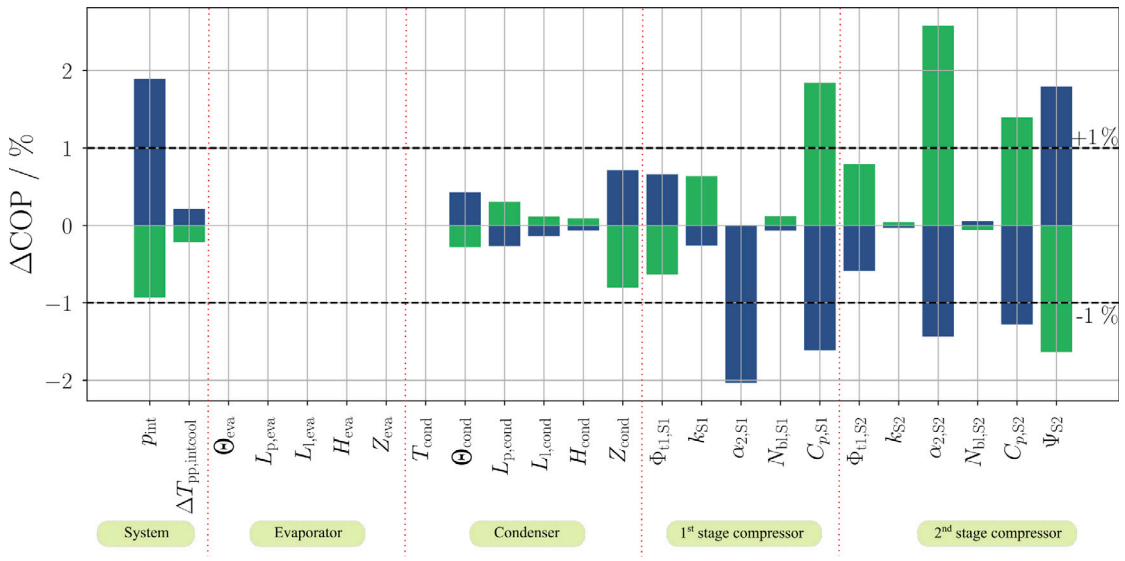

Fig. 15. Sensitivity analysis of the system COP for a variation of each one of the design variables in a range from −10% ( ) to +10% ( ).

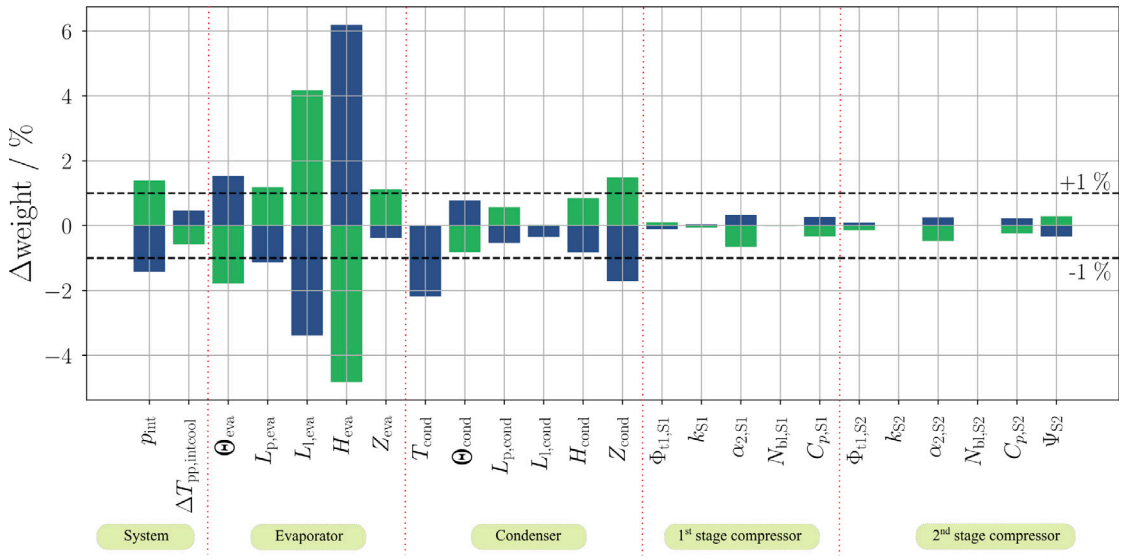

Fig. 16. Sensitivity analysis of the system weight for a variation of each one of the design variables in a range from −10% ( ) to +10% ( ).

Future work will focus on the effect of the working fluid on the optimal system design, aiming at providing guidelines for the selection of optimal refrigerants meeting the requirements dictated by the F-gas regulation [65]. The choice of the working fluid will be oriented to the class of low-GWP refrigerants, in particular to the hydrofluoroolefins, whose advantages have been investigated in Ascione et al. [61]. Furthermore, the Propulsion & Power group of the Delft University of Technology is currently commissioning the IRIS (Inverse organic Rankine cycle Integrated System) test rig. The setup is conceived to assess the performance of vapour compression cycle systems for aircraft environmental control system, and of high-speed centrifugal compressors in particular, and to validate the components and systems models developed thus far.

As a last remark, the authors want to draw attention to a numerical problem associated with the need to correctly initialize steady-state simulations of complex Modelica system models to enable the convergence of the simulation. The choice of a consistent set of initial conditions is not trivial, and it may represent a limitation when dealing with stochastic optimization algorithms since it is difficult to define *a priori* such values for each vector of design variables. Consequently, due to the limited convergence capability of the model, the resulting design space could be narrower than the actual one. To overcome this problem, future efforts will be devoted to the improvement of the integrated design optimization framework by decoupling the centrifugal compressor design from that of the entire system, using the in-house tool documented in [66]. In this way, the complexity of the set of equations describing the ECS system model will be reduced without compromising the accuracy of the compressor design.

CRediT authorship contribution statement

F. Ascione: Conceptualization, Methodology, Software development, Validation, Data curation, Writing – original draft. **P. Colonna:** Funding acquisition, Project direction, Writing – review & editing. **C.M. De Servi:** Conceptualization, Supervision, Review & editing.

Declaration of competing interest

The authors declare that they have no known competing financial interests or personal relationships that could have appeared to influence the work reported in this paper.

Data availability

The authors do not have permission to share data.

Acknowledgements

The authors gratefully acknowledge the contribution of Dr. Vincent Pommé of Airbus Helicopters for the continued support and for providing suggestions and information regarding the selection of the design point and of the VCC system configuration. The authors are also grateful to their colleague Andrea Giuffré for his advice during the development of the centrifugal compressor model. This research is supported by Aeronamic BV, by the Applied and Engineering Sciences Division (TTW) of the Dutch Organization for Scientific Research (NWO) via the Technology Program of the Ministry of Economic Affairs of the Netherlands (Grant No. 17091).

References

[1] European Commission, Flightpath 2050 Europe's Vision for Aviation: Maintaining Global Leadership and Serving Society's Needs, Technical Report, Publications Office, LU, 2011.
[2] B. Sarlioglu, C.T. Morris, More electric aircraft: Review, challenges, and opportunities for commercial transport aircraft, IEEE Trans. Transp. Electrif. 1 (1) (2015) 54–64, http://dx.doi.org/10.1016/j.ijrefrig.2009.07.006.
[3] AIR1168/8, Aircraft fuel weight penalty due to air conditioning, 2011, p. 20, http://dx.doi.org/10.4271/AIR1168/8A.
[4] A. Mannini, G. Sarri, V. Marchis, Air cycle environmental control system for helicopters: A trade-off study, in: Twelfth European Rotorcraft Forum, Garmish - Partenkirchen, 1986, p. 16.
[5] C. Zilio, G. Righetti, S. Mancin, R. Hodot, C. Sarno, V. Pomme, B. Truffart, Active and passive cooling technologies for thermal management of avionics in helicopters: Loop heat pipes and mini-vapor cycle system, Therm. Sci. Eng. Prog. 5 (2018) 107–116, http://dx.doi.org/10.1016/j.tsep.2017.11.002.
[6] L. Pang, D. Ma, K. Luo, X. Mao, Y. Yuan, Performance of an integrated thermal management system for helicopter, Energy 239 (2022) 122292, http://dx.doi.org/10.1016/j.ijrefrig.2015.01.009.
[7] A. Mannini, Vapor cycle versus air cycle environmental control system: Selection criteria on modern helicopters, in: Twentieth European Rotorcraft Forum, Amsterdam, 1994, p. 15.
[8] A. Mannini, The environmental control system for a modern helicopter: A blend of new technologies, in: Twenty-first European Rotorcraft Forum, Saint-Petersburg, Russia, 1995, p. 11.
[9] J.V. Vargas, A. Bejan, Integrative thermodynamic optimization of the environmental control system of an aircraft, Int. J. Heat Mass Transfer 44 (20) (2001) 3907–3917, http://dx.doi.org/10.1016/S0017-9310(01)00033-3.
[10] I. Pérez-Grande, T.J. Leo, Optimization of a commercial aircraft environmental control system, Appl. Therm. Eng. 22 (17) (2002) 1885–1904, http://dx.doi.org/10.1115/1.4007548.
[11] M. Sielemann, T. Giese, B. Oehler, M. Gräber, Optimization of an unconventional environmental control system architecture, SAE Int. J. Aerosp. 4 (2) (2011) 1263–1275, http://dx.doi.org/10.1155/2021/6669193.
[12] Modelica Association, Modelica Language Specification, Version 3.5, Technical Report, Modelica Association, 2021.
[13] ANSI/ASHRAE Standard 34, ASHRAE standard 34-2022 - Designation and safety classification of refrigerants, 2022.
[14] ARP731C, General requirements for application of vapor cycle refrigeration systems for aircraft, 2015, http://dx.doi.org/10.4271/ARP731C.
[15] ARP292, Air conditioning helicopter general requirements, 2014, p. 7, http://dx.doi.org/10.4271/ARP292.
[16] G.F. Hundy, Refrigeration, Air Conditioning and Heat Pumps, Butterworth-Heinemann, 2016.
[17] E.W. Lemmon, I.H. Bell, M.L. Huber, M.O. McLinden, NIST Standard Reference Database 23: Reference Fluid Thermodynamic and Transport Properties-REFPROP, Version 10.0, National Institute of Standards and Technology, 2018, http://dx.doi.org/10.18434/T4/1502528.
[18] B. Zohuri, Compact Heat Exchangers, Springer International Publishing, Cham, 2017, http://dx.doi.org/10.1007/978-3-319-29835-1.
[19] S.G. Kandlikar, Fundamental issues related to flow boiling in minichannels and microchannels, Exp. Therm Fluid Sci. 26 (2) (2002) 389–407, http://dx.doi.org/10.1016/S0894-1777(02)00150-4.
[20] R.K. Shah, D.P. Sekulić, Fundamentals of Heat Exchanger Design, John Wiley & Sons, Hoboken, NJ, 2003.
[21] M.-H. Kim, C.W. Bullard, Performance evaluation of a window room air conditioner with microchannel condensers, J. Energy Resour. Technol. 124 (1) (2022) 9, http://dx.doi.org/10.1115/1.1446072, 47-55.
[22] S. Bendapudi, J.E. Braun, E.A. Groll, A comparison of moving-boundary and finite-volume formulations for transients in centrifugal chillers, Int. J. Refrig. 31 (8) (2008) 1437–1452, http://dx.doi.org/10.1016/0017-9310(96)00116-0.
[23] H. Schmidt, A. Wellenhofer, S. Muschelknautz, J. Schmidt, F. Schmidt, D. Mewes, A. Mersmann, J. Stichlmair, L2 Two-phase gas-liquid flow, in: VDI Heat Atlas, Springer Berlin Heidelberg, Berlin, Heidelberg, 2010, pp. 1117–1180, http://dx.doi.org/10.1007/978-3-540-77877-6_78.
[24] VDI e. V., VDI Heat Atlas, Springer Berlin, Heidelberg, 2010, http://dx.doi.org/10.1007/978-3-540-77877-6.
[25] M.-H. Kim, C.W. Bullard, Air-side thermal hydraulic performance of multi-louvered fin aluminum heat exchangers, Int. J. Refrig. 25 (2002) 390–400, http://dx.doi.org/10.1016/S0140-7007(01)00025-1.
[26] Y.-J. Chang, C.-C. Wang, A generalized heat transfer correlation for louver fin geometry, Int. J. Heat Mass Transfer 40 (1997) 12, http://dx.doi.org/10.1016/0017-9310(96)00116-0.
[27] R.W. Lockhart, R.C. Martinelli, Proposed correlation of data for isothermal two-phase, two-component flow in pipes, Chem. Eng. Progr. 45 (1949) 39–48.
[28] D. Chisholm, Pressure gradients due to friction during the flow of evaporating two-phase mixtures in smooth tubes and channels, Int. J. Heat Mass Transfer 16 (2) (1973) 347–358, http://dx.doi.org/10.1016/0017-9310(73)90063-X.
[29] M.S. Yadav, S.A. Giri, V.C. Momale, Sizing analysis of louvered fin flat tube compact heat exchanger by genetic algorithm, Appl. Therm. Eng. 125 (2017) 1426–1436, http://dx.doi.org/10.1016/j.applthermaleng.2017.07.119.
[30] V. Gnielinski, On heat transfer in tubes, Int. J. Heat Mass Transfer 63 (2013) 134–140, http://dx.doi.org/10.1016/j.ijheatmasstransfer.2013.04.015.
[31] S.G. Kandlikar, A general correlation for saturated two-phase flow boiling heat transfer inside horizontal and vertical tubes, J. Heat Transfer 112 (1) (1990) 219–228, http://dx.doi.org/10.1115/1.2910348.
[32] M. Shah, A general correlation for heat transfer during film condensation inside pipes, Int. J. Heat Mass Transfer 22 (4) (1979) 547–556, http://dx.doi.org/10.1016/0017-9310(79)90058-9.
[33] W. Kast, H. Nirschl, E.S. Gaddis, K.E. Wirth, J. Stichlmair, L1 - Pressure drop in single phase flow, in: VDI Heat Atlas, Springer Berlin Heidelberg, Berlin, Heidelberg, 2010, pp. 1053–1116, http://dx.doi.org/10.1007/978-3-540-77877-6.
[34] J. Schmidt, L. Friedel, Two-phase pressure drop across sudden contractions in duct areas, Int. J. Multiph. Flow. 23 (2) (1997) 283–299, http://dx.doi.org/10.1016/S0301-9322(96)00056-0.
[35] H. Martin, N6 - Pressure drop and heat transfer in plate heat exchangers, in: VDI Heat Atlas, Springer Berlin Heidelberg, Berlin, Heidelberg, 2010, pp. 1515–1522, http://dx.doi.org/10.1016/0255-2701(95)04129-X.
[36] B. Palm, J. Claesson, Plate heat exchangers: Calculation methods for single and two-phase flow, Heat Transfer Eng. 27 (4) (2006) 88–98, http://dx.doi.org/10.1080/01457630500523949.
[37] Aspen Technology, Aspen Exchanger Design & Rating, 2008.
[38] H. Martin, A theoretical approach to predict the performance of chevron-type plate heat exchangers, Chem. Eng. Process. 35 (1996) 10, http://dx.doi.org/10.1016/0255-2701(95)04129-X.
[39] M. Cooper, Heat flow rates in saturated nucleate pool boiling-A wide-ranging examination using reduced properties, in: Advances in Heat Transfer, vol. 16, Elsevier, 1984, pp. 157–239.
[40] M.V. Casey, D. Krähenbuhl, C. Zwyssig, The design of ultra-high-speed miniature centrifugal compressors, in: European Conference on Turbomachinery Fluid Dynamics and Thermodynamics ETC, Vol. 10, Lappeenranta, Finland, 2013, p. 14.
[41] J. Schiffmann, D. Favrat, Experimental investigation of a direct driven radial compressor for domestic heat pumps, Int. J. Refrig. 32 (8) (2009) 1918–1928, http://dx.doi.org/10.1016/j.ijrefrig.2009.07.006.
[42] A. Giuffré, P. Colonna, M. Pini, The effect of size and working fluid on the multi-objective design of high-speed centrifugal compressors, Int. J. Refrig. 143 (2022) 43–56, http://dx.doi.org/10.1016/j.ijheatmasstransfer.2013.04.015.
[43] D. Rusch, M. Casey, The design space boundaries for high flow capacity centrifugal compressors, J. Turbomach. 135 (3) (2013) 031035, http://dx.doi.org/10.1115/1.4007548.
[44] T.W. von Backström, A unified correlation for slip factor in centrifugal impellers, J. Turbomach. 128 (1) (2006) 1–10, http://dx.doi.org/10.1115/1.2101853.
[45] H.W. Oh, E.S. Yoon, M.K. Chung, An optimum set of loss models for performance prediction of centrifugal compressors, Proc. Inst. Mech. Eng. A J. Power Energy 211 (4) (1997) 331–338, http://dx.doi.org/10.1243/0957650971537231.
[46] J.E. Coppage, F. Dallenbach, Study of Supersonic Radial Compressors for Refrigeration and Pressurization Systems, Technical Report, Garrett Corp Los Angeles Ca AiResearch MFG DIV, 1956.
[47] W. Jansen, A Method for Calculating the Flow in a Centrifugal Impeller When Entropy Gradient Are Present, Institution of Mechanical Engineers Internal Aerodynamics, 1970.
[48] J.P. Johnston, J. Dean, Losses in vaneless diffusers of centrifugal compressors and pumps: Analysis, experiment, and design, J. Eng. Power 88 (1) (1966) 49–60, http://dx.doi.org/10.1115/1.3678477.
[49] J.W. Daily, R.E. Nece, Chamber dimension effects on induced flow and frictional resistance of enclosed rotating disks, J. Basic Eng. 82 (1) (1960) 217–230, http://dx.doi.org/10.1115/1.4029482.

[50] R.H. Aungier, Mean streamline aerodynamic performance analysis of centrifugal compressors, J. Turbomach. 117 (3) (1995) 360–366, http://dx.doi.org/10.1016/0017-9310(96)00116-0.
[51] F. De Bellis, A. Grimaldi, D.T. Rubino, R. Amirante, E. Distaso, Accurate radial vaneless diffuser one-dimensional model, J. Eng. Gas Turb. Power 137 (8) (2015) 082603, http://dx.doi.org/10.1115/1.4029482.
[52] J.D. Stanitz, One-dimensional Compressible Flow in Vaneless Diffusers of Radial- and Mixed-flow Centrifugal Compressors, Including Effects of Friction, Heat Transfer and Area Change, NACA-TN-2610, NASA, 1952.
[53] O. Dubitsky, D. Japikse, Vaneless diffuser advanced model, J. Turbomach. 130 (1) (2008) 011020, http://dx.doi.org/10.1115/1.3454631.
[54] J. Tiainen, A. Jaatinen-Värri, A. Grönman, P. Sallinen, J. Honkatukia, T. Hartikainen, Validation of the axial thrust estimation method for radial turbomachines, in: C. Xu (Ed.), Int. J. Rotating Mach. 2021 (2021) 1–18, http://dx.doi.org/10.1155/2021/6669193.
[55] H. Nguyen-Schäfer, Rotordynamics of Automotive Turbochargers, Springer Berlin Heidelberg, Berlin, Heidelberg, 2012, http://dx.doi.org/10.1007/978-3-642-27518-0.
[56] D. Japikse, Centrifugal Compressor Design and Performance, Concepts Eti, 1996.
[57] J. Larjola, Radiaalikompressorin Suunnittelun Perusteet (in Finnish),(Centrifugal Compressors, the Fundamentals of Design), Research Report EN B-61, Lappeenranta University of Technology, Department of Energy Technology, 1988.
[58] ASME B31.5, Refrigeration Piping and Heat Transfer Components, ASME, 2019.
[59] CS-25 Amendment 3, Certification Specifications for Large Aeroplanes, European Aviation Safety Agency, 2017, p. 617.
[60] Dassault Systèmes AB, Dymola: Dynamic Modeling laboratory, Lund, Sweden, 2022.
[61] F. Ascione, C.M.D. Servi, O. Meijer, V. Pommé, P. Colonna, Assessment of an inverse organic Rankine cycle system for the ECS of a large rotorcraft adopting a high-speed centrifugal compressor and a low GWP refrigerant, in: T.U. of Munich (Ed.), Proceedings of the 6th International Seminar on ORC Power Systems, Technical University of Munich, 2021, http://dx.doi.org/10.14459/2021mp1633127.
[62] A. Zucht, AKG Group, Personal communication, 2022.
[63] J. Blank, K. Deb, Pymoo: Multi-objective optimization in python, IEEE Access 8 (2020) 89497–89509, http://dx.doi.org/10.1016/0017-9310(96)00116-0.
[64] A. Saltelli, M. Ratto, T. Andres, F. Campolongo, J. Cariboni, D. Gatelli, M. Saisana, S. Tarantola, Global Sensitivity Analysis: the Primer, John Wiley & Sons, 2008.
[65] European Parliament and Council, Regulation (EU) No 517/2014 on fluorinated greenhouse gases, Official J. Eur. Union L150 (2014) 195–230.
[66] A. Giuffré, P. Colonna, M. Pini, Design optimization of a high-speed twin-stage compressor for next-gen aircraft environmental control system, J. Eng. Gas Turb. Power 145 (3) (2022) http://dx.doi.org/10.1115/1.4056022, 031017.